Epigenomic Diversity of Cortical Projection Neurons in the Mouse Brain

Zhuzhu Zhang[1*], Jingtian Zhou[1,2*], Pengcheng Tan[1,3], Yan Pang[4], Angeline Rivkin[1], Megan A. Kirchgessner[4,5], Elora Williams[6], Cheng-Ta Lee[7], Hanqing Liu[1,8], Alexis D. Franklin[4], Paula Assakura Miyazaki[4], Anna Bartlett[1], Andrew Aldridge[1], Minh Vu[4], Lara Boggeman[9], Conor Fitzpatrick[9], Joseph R. Nery[1], Rosa G. Castanon[1], Mohammad Rashid[4], Matthew Jacobs[4], Tony Ito[4], Bertha Dominguez[7], Sheng-Yong Niu[1], Jared B. Smith[6], Caz O'Connor[9], Kuo-Fen Lee[7], Xin Jin[6], Eran A. Mukamel[10], M. Margarita Behrens[11], Joseph R. Ecker[1,12†], and Edward M. Callaway[4†]

[1]Genomic Analysis Laboratory, The Salk Institute for Biological Studies, La Jolla, CA 92037

[2]Bioinformatics and Systems Biology Program, University of California San Diego, La Jolla, CA 92093

[3]School of Pharmaceutical Sciences, Tsinghua University, Beijing, China, 100084

[4]Systems Neurobiology Laboratories, The Salk Institute for Biological Studies, La Jolla, CA 92037

[5]Neurosciences Graduate Program, University of California, San Diego, La Jolla, CA 92093

[6]Molecular Neurobiology Laboratory, The Salk Institute for Biological Studies, La Jolla, CA 92037

[7]Peptide Biology Laboratories, The Salk Institute for Biological Studies, La Jolla, CA 92037

[8]Division of Biological Sciences, University of California San Diego, La Jolla, CA 92093

[9]Flow Cytometry Core Facility, The Salk Institute for Biological Studies, La Jolla, CA 92037

[10]Department of Cognitive Science, University of California, San Diego, La Jolla, CA 92037

[11]Computational Neurobiology Laboratory, The Salk Institute for Biological Studies, La Jolla, CA 92037

[12]Howard Hughes Medical Institute, The Salk Institute for Biological Studies, La Jolla, CA 92037

[†]Correspondence: callaway@salk.edu, ecker@salk.edu

*These authors contributed equally

Summary

Neuronal cell types are classically defined by their molecular properties, anatomy, and functions. While recent advances in single-cell genomics have led to high-resolution molecular characterization of cell type diversity in the brain, neuronal cell types are often studied out of the context of their anatomical properties. To better understand the relationship between molecular and anatomical features defining cortical neurons, we combined retrograde labeling with single-nucleus DNA methylation sequencing to link epigenomic properties of cell types to neuronal projections. We examined 11,827 single neocortical neurons from 63 cortico-cortical (CC) and cortico-subcortical long-distance projections. Our results revealed unique epigenetic signatures of projection neurons that correspond to their laminar and regional location and projection patterns. Based on their epigenomes, intra-telencephalic (IT) cells projecting to different cortical targets could be further distinguished, and some layer 5 neurons projecting to extra-telencephalic targets (L5-ET) formed separate subclusters that aligned with their axonal projections. Such separation varied between cortical areas, suggesting area-specific differences in L5-ET subtypes, which were further validated by anatomical studies. Surprisingly, a population of CC projection neurons clustered with L5-ET rather than IT neurons, suggesting a previously undescribed population of L5-ET cortical neurons projecting to both targets (L5-ET+CC). We verified the existence of these neurons by labeling the axon terminals of CC projection neurons and observed clear labeling in ET targets including thalamus, superior colliculus, and pons. These findings highlight the power of single-cell epigenomic approaches to connect the molecular properties of neurons with their anatomical and projection properties.

46 **Main Text**

47 The mammalian brain is a complex system consisting of multiple types of neurons with diverse
48 morphology, physiology, connections, gene expression, and epigenetic modifications. Identifying
49 brain cell types and how they interact is critical to understanding the neural mechanisms that
50 underlie brain function. During the last decade, these efforts have been facilitated by the advent of
51 molecular, genetic and viral tools for allowing genetic access and manipulation of specific cell
52 types[1,2]. Available evidence suggests, however, that there are far more cell types than can presently
53 be accessed genetically. Moreover, the correspondence between molecular cell types and neuronal
54 populations defined by connectivity are largely unknown.

55

56 Single-cell technologies deconvolve mammalian brains into molecularly defined cell clusters
57 corresponding to putative neuron types[3]. Among these technologies, single nucleus methylation
58 sequencing (snmC-Seq) applied to neurons has the unique ability to allow identification of
59 potential regulatory elements and a prediction of gene expression in the same cells. This is because
60 methylation at non-CG (CH; H= A, T, C) dinucleotides (mCH) of the gene body is inversely
61 correlated with RNA expression, and methylation at both CG dinucleotides (mCG) and CH
62 dinucleotides can be used to identify gene regulatory elements associated with gene expression[4–
63 6]. Furthermore, CH methylation accumulates and CG methylation reconfigures during cortical
64 synaptic development, suggesting possible links between epigenetics and connectivity[7,8].

65

66 Previous single-cell analyses have revealed transcriptomic clusters and linked them to neuron
67 types with different projection patterns in a few particular brain regions[9–12]. For the cerebral cortex,
68 the most prominent molecular distinction related to projection targets is the separation of cortical

69 neurons into distinct and apparently non-overlapping IT and L5-ET (also called pyramidal tract,
70 PT) groups. In some cases L5-ET cells have been further divided based on both gene expression
71 and corresponding axon projections[9]. While the separation of L5-IT and ET neurons appears to be
72 conserved across cortical areas[13] and species[14], a systematic analysis of the relationships between
73 a larger set of projection targets and molecular identities across multiple cortical areas has not been
74 conducted. To what extent cortical projection neuron types can be further distinguished or divided
75 by incorporating anatomical information with molecular analyses, and whether these cell types
76 and correspondences are conserved across cortical areas is unclear. Ultimately, the use of methods
77 that can classify cell types and predict regulatory elements, such as snmC-seq, will be critical to
78 understanding cell type and/or projection type specific regulatory mechanisms.
79
80 To address these questions we developed Epi-Retro-Seq, which applies snmC-Seq[15] to neurons
81 dissected from cortical source regions which were labeled based on their long distance projections
82 to specific cortical and subcortical targets. We analyzed the methylomes of 11,827 single neurons
83 from eight cortical areas projecting to ten target regions. This dataset enabled us to quantify the
84 epigenetic differences between cortical projection neurons, to identify specific genes and
85 regulatory elements in projection neurons, to study the relationships between cortical projection
86 neurons and molecular cell types, and to identify a previously unknown neuron type making
87 projections to both cortical and ET targets.
88

Results

Epi-Retro-Seq of 63 cortical projections

To obtain a comprehensive view of the molecular diversity among cortical projection neurons we performed Epi-Retro-Seq, which combines retrograde tracing with epigenomic profiling. We characterized projection neurons from eight cortical areas ("source") spanning the anterior-to-posterior extent of the mouse cortex that project to ten cortical or subcortical regions ("target") (Fig. 1a), covering overall 26 CC projections and 37 cortico-subcortical projections (Supplementary Table 1). In Epi-Retro-Seq, the retrograde viral tracer rAAV2-retro-Cre is injected in the target region in an INTACT mouse[4], turning on Cre-dependent nuclear-GFP expression in neurons that project to the injected target, throughout the mouse brain. The brain is then sectioned into eighteen 600-micron coronal slices, and the source regions of interest are dissected from each slice (see Methods). Nuclei are sampled from at least 4 mice (2 male and 2 female) for each projection target (except AI→pons - 2 male mice only). Nuclei from each of the dissected source regions are prepared, from which $GFP^+/NeuN^+$ nuclei (the GFP-labeled projection neurons) are isolated as single nuclei using fluorescence activated nuclei sorting (FANS) and assayed using snmC-Seq2[15] to profile their genome-wide DNA methylation signatures. The ten injected target regions include four cortical areas [the primary motor cortex (MOp), primary somatosensory cortex (SSp), anterior cingulate area (ACA), and primary visual cortex (VISp)], and six major subcortical structures [the striatum (STR), thalamus (TH), superior colliculus (SC), ventral tegmental area and substantia nigra (VTA+SN), pons, and medulla (MY)]. Each of the eight source cortical regions [MOp, SSp, ACA, agranular insular cortex (AI), retrosplenial cortex (RSP), auditory cortex (AUDp+AUDd+AUDv), posterior parietal cortex (PTLp), and visual cortex (VISp+VISpm+VISl+VISli)] were hand dissected from one or two coronal slices following the

112 Allen Mouse Common Coordinate Framework (CCF), Reference Atlas, Version 3 (2015)
113 (Extended Data Fig. 1).
114
115 **Methylation landscape of cortical projection neurons**
116 We assayed approximately 384 nuclei from each projection (except the MOp→SSp projection
117 from which 768 nuclei were assayed). After removing the low-quality cells, potential doublets,
118 and glial cells (possibly due to false NeuN positives in FANS), we obtained high-quality single
119 methylomes for 11,827 cortical projection neurons (Extended Data Fig. 2). The level of CH
120 methylation in each single nucleus was computed across the genome using 100 kb genomic bins
121 and used to perform unsupervised clustering of the projection neurons. Overall, the cortical
122 projection neuron clusters were annotated into 10 major cell types (Fig. 1b) based on the reduced
123 levels of gene body mCH, a proxy for gene expression, of known marker genes (Extended Data
124 Fig. 2f). It should be noted that 361 neurons (3.05%) fell into the inhibitory neuron cluster, likely
125 representing false-positives possibly, due to either labeling of neurons by AAV that leaked into
126 cortical areas above subcortical injection sites (mostly from areas above TH injections), or
127 insufficient gating stringency during FANS, allowing inclusion of GFP-negative nuclei. This low
128 error rate allows a rough estimate of the likely erroneous contributions from other cell types.
129 Within each cell type cluster, excitatory neurons but not inhibitory neurons from different cortical
130 regions were further separated from each other (Fig. 1c), demonstrating that such separations in
131 excitatory neuron clusters were not due to technical effects but instead represented the distinct
132 spatial DNA methylation patterns in cortical projection neurons. As can be seen from the t-SNE
133 visualization (Fig. 1d), neurons projecting to different target regions were more similar within each
134 cluster than neurons from different source regions, indicating that they shared a more similar DNA

135 methylation landscape. Neighbor enrichment scores were used to quantify the variations of DNA
136 methylation that originated from different cell types, cortical spatial regions, and projection targets
137 (see Methods). Neurons from the same cluster occupied highly similar regions in the dimension
138 reduction space (neighbor enrichment score was near 1). Scores were also high for comparisons
139 across neurons from the same source, followed by projections to the same target. Scores were near
140 chance for biological replicates (Fig. 1h).
141
142 Next, we integrated our data with the single-nuclei methylation data that were dissected and
143 sorted from some of the same cortical regions but without enrichment of specific projections (Liu
144 et al., companion paper #9). We observed a close agreement of the major cell types (Fig. 1e) and
145 source regions (Fig. 1f) between these two datasets. Given the increased number of cells, different
146 source regions became better demarcated on t-SNE (Fig. 1f). Compared with unbiased snmC-seq2
147 profiling, Epi-Retro-seq dataset also contains information about the neuronal projection targets
148 revealed by retrograde tracing (Fig. 1g). This enabled enrichment of rare types of projection
149 neurons and analysis of the methylation patterns of neurons projecting to different brain regions.
150
151 Although neurons projecting to different target regions were not completely separated on t-SNE,
152 we observed an explicit enrichment of CC and cortico-striatal projection neurons in IT clusters
153 (L2/3, L4, L5-IT, L6-IT, and Claustrum (CLA)), separated from neurons that project to the
154 remaining structures outside the telencephalon which were categorized as L5-ET neurons (Fig. 1j,
155 Extended Data Fig. 3) As expected, many cortico-thalamic projecting neurons were also found in
156 the L6-CT cluster (Fig. 1j, Extended Data Fig. 3). These enrichment patterns are consistent with

157 our knowledge about laminar enrichment of the projection neurons, which reflects the high quality
158 of our retrogradely labeled single-nuclei methylation dataset.
159
160 To further quantify methylation differences between neurons from different source regions or
161 projecting to different target regions, we made comparisons across source pairs or target pairs. For
162 each pair of interest, area under the curve of receiver operating characteristic (AUROC) was
163 calculated to score the level of separation between the two groups of projection neurons.
164 Specifically, a logistic regression model was trained using normalized gene body mCH as features
165 to predict which group a cell belongs to. By training the model in one biological replicate and
166 testing on the other, the performance was measured by AUROC. By comparing each pair of
167 sources or targets, we found that most neurons dissected from different source regions could be
168 separated with AUROC > 0.9 (Fig. 1i). Most of the neurons projecting to different target regions
169 were also separable by mCH in this supervised setting (Fig. 1i), although they were closely mixed
170 in the unsupervised embeddings (Fig. 1d). These findings indicate that nearly all of the different
171 types of projection neurons that were profiled have differences in their epigenomes.
172
173 **Epigenetic diversity of IT neurons projecting to different cortical targets**
174 As described above, assessment of the entire Epi-Retro-Seq dataset revealed clear and expected
175 differences in the neuron clusters occupied by neurons projecting to IT versus ET targets, and these
176 differences were conserved across source areas. However, neurons projecting to different IT or ET
177 targets did not uniquely separate into distinct clusters when analyzed at the level of the entire cell
178 population. Nevertheless, we were able to detect projection-dependent quantitative differences in

179 the levels of DNA methylation. Further analyses of these quantitative differences, described below,
180 allowed assessment of possible organizational principles that might exist in the relationships
181 between DNA methylation, projections targets, and sources, including both areal and laminar
182 sources.
183
184 In total, 42.6% of the cortical projection neurons profiled in our Epi-Retro-Seq data were
185 identified as IT, and annotated according to their presumptive cortical layers (Fig. 1b). We next
186 aimed to disentangle the contribution of the cortical area in which cell bodies were located versus
187 their cortical projection targets, to the variation of their DNA methylation profiles. We focused on
188 26 CC projections from 8 cortical areas to 4 different cortical targets. AUROC scores were used
189 to evaluate epigenetic relationships between cortical neurons projecting to different cortical targets.
190 All possible pairs of 4 cortical targets were assessed for each of the 8 sources to generate 29
191 AUROC scores, organized according to projection target pairs (Fig. 2a, Extended Data Fig. 4a, c).
192 Significant differences were observed between projection target pairs when assessed across source
193 areas (p=6.8e-3, Kruskal-Wallis test), but not between cortical areas when assessed across target
194 pairs (p=0.3, Kruskal-Wallis test). Among the six projection target pairs examined, neurons
195 projecting to MOp versus ACA were overall most distinguishable (average AUROC = 0.902),
196 followed by neurons projecting to ACA versus VISp (average AUROC = 0.887), while neurons
197 that project to SSp versus ACA were the least separable (average AUROC = 0.693) (Fig. 2a). In
198 addition, for each target pair, the performance of the predictive model varied among neurons from
199 different source cortical regions (Fig. 2a, Extended Data Fig. 4a, c).
200

201 Together, these analyses suggest that epigenetic differences between CC projection neurons
202 depend on a combination of both the specific targets to which neurons project and the source region
203 where the neurons reside. For example, we further evaluated the variability of mCH profiles among
204 AUD IT neurons projecting to different targets and found that AUD→SSp neurons were better
205 separated from AUD→VISp neurons (AUROC = 0.94; Fig.2b, e) than from AUD→ACA neurons
206 (AUROC = 0.709; Fig. 2c, e). t-SNE plots color-coded according to these same projection
207 comparisons (Fig. 2b, c) or according to annotated layers (Fig. 2d) allow visualization of the extent
208 to which these neurons differ. In addition to the apparent greater separability of AUD→SSP versus
209 AUD→VISp than AUD→SSP versus AUD→ACA neurons, it can be seen that the distinctions
210 between these projections did not stem from different distributions across layers (Fig. 2d). This
211 demonstrates that the level of epigenetic differences between AUD IT neurons varies depending
212 on their projection targets. On the other hand, when comparing neurons from different sources
213 projecting to the same target pair, we observed different levels of distinguishability in our models.
214 For example, while MOp-projecting versus ACA-projecting neurons were more distinguishable
215 (i.e. higher AUROC scores) than SSp-projecting versus ACA-projecting neurons, we observed
216 variation of the AUROC scores across different source regions for both target pairs (Fig. 2f, g).
217
218 To further validate that the differences in separability across regions resulted from biological
219 differences rather than limited sample sizes for some regions, we trained our predictive model
220 between two targets using neurons from one source region and then tested the performance of the
221 model on another source region. These analyses also allowed evaluation of whether the same
222 epigenetic differences that distinguished target pairs for one source area might be conserved across
223 source areas. As expected, the performances of the cross-source-region models in distinguishing

two projection targets were usually less than the same-source-region models (Fig. 2h, i, Extended Data Fig. 4b, d). Nevertheless, many target pairs that were distinguishable for the within-source models were also distinguishable with the cross-source models (Fig. 2h, i, Extended Data Fig. 4b, d), indicating conservation of target pair epigenetic differences across sources. Interestingly, the performance of models trained on any particular region varied in their ability to predict projections from other regions. For example, the model trained on data from AUD performed better in distinguishing VIS→MOp versus VIS→ACA neurons than the models trained on RSP, PTLp, or SSp (Fig. 2h). This suggests that AUD and VIS neurons are more similar to each other in the molecular markers that distinguish neurons projecting to MOp versus ACA than other cortical areas. These results indicate that cortical regions might form different groups with shared correlations between molecular markers and projection targets.

In addition, the level of distinguishability between two cortical targets appeared to be similar across layers (Fig. 2j, Extended Data Fig. 5a, b). By training and testing the predictive models in each layer separately, we observed higher distinguishability between ACA-projecting versus VISp-projecting neurons across all layers than between SSp-projecting versus ACA-projecting in all layers in almost all source regions (Fig. 2j, k). We further tested if cross-layer-trained models could distinguish the projection targets (see Methods), and observed that the performance was generally comparable to within-layer models (Extended Data Fig. 5c, d). These results suggest that there may be shared epigenetic signatures across layers that contribute to correlations with the projection targets.

246 To better understand the biology underlying the epigenetic signatures that distinguish different
247 cortical IT projection neurons, we identified differentially methylated genes at CH sites (CH-
248 DMGs) between different pairs of CC projection neurons in each source region using hierarchical
249 linear models. In total, 1830 CH-DMGs were identified (Supplementary Table 3), among which
250 1,623 (88.7%) were statistically significant in only one source region, and 207 (11.3%) were
251 differentially methylated in more than one source region (some examples shown in Fig. 2l). That
252 the vast majority of CH-DMGs were unique to one source region, suggests that different genes
253 may participate in defining projections from different source regions. Gene ontology (GO)
254 enrichment analysis revealed that CH-DMGs were enriched for genes that participate in
255 intracellular transport, regulation of synapse structure, etc. (Fig. 2m), all relevant for influencing
256 neuronal projections. For example, Bassoon (*Bsn*) is differentially methylated between MOp-
257 projecting and SSp-projecting neurons in ACA, AUD, and VIS (Fig. 2l). It encodes a presynaptic
258 cytomatrix protein expressed primarily in neurons, and is essential in regulation of
259 neurotransmitter release[16]. *Scn2a1* encodes a voltage dependent sodium channel protein and is
260 differentially methylated between SSp-projecting and VISp-projecting neurons in ACA, AI, AUD,
261 and PTLp (Fig. 2l). This channel regulates neuronal excitability and variants are associated with
262 autism and seizure disorders[17].
263

264 **Epigenetically distinct subpopulations of L5-ET neurons**

265 In our Epi-Retro-Seq data, 5 out of the 10 profiled projection targets are ET. In particular, L5-ET
266 neurons are the most abundant cell population in our datasets (4,176 (35.3%) single neurons), and
267 are 6.3 fold enriched in Epi-Retro-Seq compared to the total number of neurons observed in
268 unbiased snmC-seq2 profiling. This level of L5-ET neuron enrichment provides us with a unique

269 opportunity to more closely investigate subpopulations of L5-ET neurons. In unsupervised
270 clustering using genome-wide mCH levels measured in 100 kb genomic bins, L5-ET neurons
271 further segregated into 15 subclusters upon uniform manifold approximation and projection
272 (UMAP) embedding (Fig. 3a). Much of the separation between subclusters was driven by the
273 source location of the neurons, as neurons from different source regions were clearly separated on
274 the UMAP (Fig. 3b) and each of the subclusters consists of neurons mostly from one or two source
275 regions (Extended Data Fig. 6a). In particular, RSP and AI each formed their own specific
276 subcluster (cluster 13 and 3, respectively; Extended Data Fig. 6a, b). The similarities and
277 differences between L5-ET neurons from different source regions were quantified using
278 hierarchical clustering (Fig. 3c). The genome-wide mCH similarity is highest between MOp and
279 SSp, followed by between VIS and AUD, and between PTLp and ACA. AI and RSP were more
280 distinct; in particular, RSP was well separated from the remaining cortical regions. These
281 similarities between source regions were not well explained by their spatial proximity anterior-
282 posteriorly or medial-laterally, but better correlated with the anatomical and functional
283 connectivity between these regions. For example, MOp and SSp are components of the somatic
284 sensorimotor subnetwork, while AUD, VIS, ACA, and PTLp are components of the medial
285 subnetwork that channels information between sensory areas (that include VISp and AUD) and
286 higher order association areas (that include PTLp and ACA)[18].
287
288 To further explore the molecular identity of these L5-ET subclusters, we used gene body mCH
289 levels to identify cluster-specific genes. In total 2,675 CH-DMGs were identified in pairwise
290 comparisons between subclusters (Fig. 3d, Supplementary Table 4; examples in Extended Data
291 Fig. 6c), indicating that these genes have cluster-specific expression patterns. Gene ontology (GO)

292 enrichment analysis revealed that these L5-ET subcluster CH-DMGs were enriched in genes
293 involved in cell communication, neurogenesis, cell morphogenesis, and axon guidance (Fig. 3e,
294 Supplementary Table 4).
295
296 In addition to identification of cluster-specific gene markers using gene body mCH, a powerful
297 and unique advantage of methylation profiling is that cis-elements that regulate the marker genes
298 can be predicted based on CG methylation. Differentially CG methylated regions (CG-DMRs)
299 between clusters reliably mark cis-regulatory elements across the whole genome (not limited to
300 gene bodies). Here, we identified 341,748 CG-DMRs that were hypo-methylated in the
301 corresponding L5-ET subclusters (Fig. 3f, Supplementary Table 5). The average length of CG-
302 DMRs was 227 bp, and 84.9% of them were distal elements that located more than 5kb from the
303 annotated transcription start sites (TSSs).
304
305 The level of mCH at gene bodies is inversely correlated with gene expression, while the level of
306 mCG at gene regulatory elements, such as promoters and enhancers, is inversely correlated with
307 their regulatory activities. These relationships allowed us to use a gene regulatory network-based
308 method to integrate this information and identify transcription factors (TFs) that might function as
309 key regulators in each subcluster (see Methods; Fig. 3g). Specifically, in this network the nodes
310 were genes (including TFs), while the edges connected the TFs to their potential target genes based
311 on the TF binding motifs in CG-DMRs surrounding the TSSs. The weights of the nodes and edges
312 were set according to the predicted expression levels (gene body mCH) of the genes. After
313 applying a PageRank algorithm to score the genes in the network, we identified TFs that were
314 potentially highly expressed and may regulate many other highly expressed genes in a subset of

315 L5-ET clusters. This method combined the advantages of differential expression and motif
316 enrichment analysis (Extended Data Fig. 6d, e), and enabled us to find TFs that may be expressed
317 among a family of TFs sharing similar motifs[19]. For example, *Rora* (RAR Related Orphan
318 Receptor A), a transcriptional activator, was scored as one of the top TFs and is hypo-CH-
319 methylated in clusters 1, 8, and 13, and especially in cluster 8 (Fig. 3h, Extended Data Fig. 6d),
320 indicating its potential expression. The binding motif of RORA was also enriched in the CG-DMRs
321 of these same clusters, suggesting that RORA may bind to cis-regulatory elements that in turn
322 regulate a set of predicted downstream target genes. Many of these target genes are related to brain
323 functions and also hypo-methylated in cluster 8 (Extended Data Fig. 6f). For example, one of its
324 predicted downstream target genes, *Astn1* (Astrotactin 1) is also hypo-CH-methylated in cluster 8
325 and encodes for a neuronal adhesion molecule, showing clear correlation between *Rora* and *Astn1*
326 expression inferred from gene-body mCH (Fig. 3i).
327
328 **Subclusters of L5-ET neurons project to different targets**
329 Our analyses of cortical IT neurons revealed epigenetic differences between neurons that related
330 to both their cortical locations and their projection targets. Although the separation of L5-ET
331 neuron subclusters was mostly driven by the source regions, neurons from the same source regions
332 (except AI and RSP) distributed into more than one subcluster (Fig. 3a, b Extended Data Fig. 6b),
333 prompting us to ask whether some of the differences between L5-ET subclusters also correspond
334 to the different projection targets. To investigate this, we performed another iteration of clustering
335 analysis using L5-ET cell data from each of the source regions separately, and identified finer L5-
336 ET subclusters within each source region (Extended Data Fig. 7a). Consistent with these
337 subclusters being related to true differences between putative cell types, all pairs of subclusters

338 had more than 5 differentially CH-methylated 100 kb bins (CH-DMBs) (298 CH-DMBs on
339 average).
340
341 We then examined whether neurons projecting to a specific target region were enriched or
342 depleted in any of the subclusters (Extended Data Fig. 7c, d). Among all comparisons between
343 projection targets and subclusters, neurons projecting to medulla (MY) were most distinct. SSp
344 L5-ET neurons further segregated into seven subclusters (Fig. 4a), among which SSp→MY
345 neurons showed a clear enrichment in subcluster 0 (FDR = 1.72E-2, Wald test; Fig. 4b, c).
346 Similarly, we identified seven subclusters of MOp L5-ET neurons, and MOp→MY neurons were
347 also significantly enriched in one of the subclusters (FDR = 6.81E-3, Wald test; Extended Data
348 Fig. 7c, d). Moreover, MY-projecting neurons were robustly distinguished from other L5-ET
349 neurons in our prediction models for both MOp and SSp (average AUROC = 0.929, 0.860; Fig.
350 4d, Extended Data Fig. 8a). Together, these analyses suggest that MY-projecting L5-ET neurons
351 are more distinct than L5-ET neurons projecting to the other targets that were assessed.
352
353 To investigate which genes drive the observed epigenomic differences between MY-projecting
354 L5-ET neurons and other L5-ET neurons, we compared the gene body CH methylation profiles of
355 MY-projecting L5-ET neurons to L5-ET neurons projecting to each of the other ET targets. In
356 total, we identified 1,380 CH-DMGs between MOp→MY L5-ET neurons and at least one of the
357 other ET projections (Fig. 4e, Supplementary Table 6). The majority of CH-DMGs were shared
358 across the other ET projections. Specifically, among the 939 CH-DMGs that were hypo-
359 methylated in MY-projecting neurons, 98 (10.4%) were universally hyper-methylated in all the
360 other ET projections; Among the 441 CH-DMGs that were hyper-methylated in MY-projecting

361 neurons, 85 (19.3%) were hypo-methylated in all the other ET projections. These results suggest
362 that there are shared molecular differences that distinguish MOp→MY neurons from MOp
363 neurons that project to VTA, SC, Pons, or TH. Similarly, 285 CH-DMGs were identified between
364 SSp→MY L5-ET neurons and at least one of the other ET projections (Fig. 4f, Supplementary
365 Table 6), among them 111 were hypo-methylated in SSp→MY neurons and 174 were hyper-
366 methylated.
367
368 In total, 171 CH-DMGs were identified in both MOp→MY and SSp→MY neurons (a few
369 examples highlighted in Fig. 4e, f), suggesting a general regulatory mechanism that may be shared
370 by different cortical regions. Accordingly, models trained in either MOp or SSp to distinguish
371 MY-projecting neurons usually performed well when tested in the other region (Extended Data
372 Fig. 8b). Indeed, similar enrichment of MY-projecting neurons in subpopulations of L5-ET
373 neurons has been reported in ALM using scRNA-seq (retro-seq)[13]. To compare these observations,
374 we used gene body mCH as a proxy for gene expression to integrate our L5-ET Epi-Retro-Seq
375 data with the ALM retro-seq data. Joint t-SNE showed that the MY-projecting L5-ET neurons
376 were enriched in the same subcluster (Extended Data Fig. 9). *Slco2a1*, a marker gene of the ALM
377 MY-projecting cluster[9,13] is hypo-methylated in MOp→MY but not in SSp→MY neurons
378 (Extended Data Fig. 9h). We identified *Astn2* as a marker gene for the MY-projecting L5-ET
379 cluster in both MOp and SSp (Extended Data Fig. 9i). ASTN2 mediates the recycling of neuronal
380 cell adhesion molecule ASTN1 in migrating neurons, and its deletion has been associated with
381 schizophrenia. This suggests that, compared to other L5-ET neurons, MY-projecting neurons have
382 distinct molecular properties, and these distinctions are likely shared across several cortical regions.
383

384 In addition to the MY-projecting L5-ET neurons, we also observed differences in genome-wide
385 mCH profiles between other ET projections. For example, L5-ET neurons in AI were segregated
386 into five subclusters (Fig. 4g), and AI→Pons and AI→SC neurons were enriched in different
387 subclusters (Fig. 4h, i, Extended Data Fig. 8c). In contrast, AI→Pons and AI→TH neurons were
388 enriched in similar subclusters (Extended Data Fig. 8c). Analysis of gene body mCH identified
389 145 CH-DMGs that were differentially methylated between AI→SC neurons versus AI→Pons,
390 while most of them had similar expression patterns between AI→Pons and AI→TH neurons (Fig.
391 4j). Together, the results suggest that AI→Pons neurons are more distinct from AI→SC neurons
392 and are similar to AI→TH neurons.
393
394 In contrast to the conservation across cortical areas ALM, MOp, and SSp for differences related
395 to projections to MY, differences between Pons-projecting and SC-projecting neurons were not
396 conserved across all cortical areas. We trained a prediction model using mCH profiles to
397 distinguish Pons- versus SC-projecting neurons from different source regions. The model
398 performed well in distinguishing the two projections from cortical regions AI (AUROC = 0.939)
399 and VIS (AUROC = 0.868), but performed poorly in PTLp neurons (AUROC = 0.726) (Extended
400 Data Fig. 8a). The AUROC scores were correlated with the counts of CH-DMGs identified
401 between SC-projecting versus Pons-projecting neurons in the corresponding source regions
402 (Spearman r=0.683). This suggests that the differences between Pons-projecting and SC-projecting
403 neurons vary across the cortex.
404
405 From these observations, we hypothesized that the level of the epigenetic differences between
406 the two projections might be correlated with the percentage of neurons that simultaneously project

407 to both Pons and SC, which might vary between different cortical regions. That is, in a cortical
408 area where more neurons project to both Pons and SC, the epigenetic profiles of Pons- and SC-
409 projecting neurons might be expected to be less distinguishable in our data, and vice versa. To test
410 this hypothesis, we performed double retrograde labeling of Pons and SC, and counted in each
411 cortical source region the number of neurons labeled only by the tracer injected into Pons, only
412 SC, or both (Supplementary Table 7). As our hypothesis predicted, PTLp had the highest
413 percentage of double-labeled neurons, and in general the AUROC score from our model was
414 negatively correlated with the percentage of double-labeled cells (Spearman r=-0.829, p=0.04)
415 across the cortical regions (Fig. 4k). These correspondences are weak, however, for most source
416 regions, so the correlation is driven primarily by the data from PTLp.
417
418 **Previously undescribed L5-ET+CC neurons**
419 Intriguingly, we noticed more than 30 VISp-projecting neurons in L5-ET clusters from ACA and
420 RSP datasets (Fig. 5a, b). Since neurons in the L5-ET cluster are likely to project to ET targets,
421 this finding suggested that some L5 neurons might project to both cortical and ET targets. These
422 neurons were enriched specifically in one subcluster in ACA and RSP, respectively (FDR = 9.82E-
423 5, 2.45E-3, Wald test; Fig. 5a-d). This type of subcluster in both RSP and ACA was marked by
424 *Ubn2*, a highly expressed gene in visual systems, and many other genes also distinguished this
425 cluster in either region.
426
427 Single neurons projecting to both a cortical target, visual area MT, and a subcortical target, SC,
428 have been observed in layer 6 of primate VISp[20,21]. However, since ET neurons represent a small
429 percentage of primate neurons, these dual-projection neurons are extremely rare; they are also

430 located in layer 6 rather than layer 5 making it difficult to predict whether they might be genetically
431 more closely related to ET or to IT neurons, whether they might project to additional subcortical
432 targets, or whether they might be unique to primates. To anatomically validate this finding in mice,
433 we injected AAVretro-Cre in VISp and AAV-flex-GFP (Cre-dependent GFP) in RSP in three mice
434 (Fig. 5e). This resulted in labeling of the complete axonal and dendritic arbors of RSP→VISp
435 neurons such that their long-distance projections to locations other than VISp could be assessed.
436 We observed strong GFP labeling of axon terminals in subcortical ET regions, including TH, SC,
437 and Pons, in all three mice (Fig. 5f). These results indicate that single neurons in L5 of RSP can
438 project simultaneously to both cortical and subcortical, ET targets in mice. Because these cells
439 genetically cluster with L5-ET cells, we consider them a subtype of L5-ET cells that we refer to
440 as L5-ET+CC. We do not use the term L5-ET+IT because many L5-ET neurons are known to
441 project to another part of the telencephalon, the striatum.
442
443 **Discussion**
444 Here, we have quantitatively analyzed and compared the methylation of mouse cortical neurons
445 projecting to different cortical and subcortical target regions. We identified genes that were
446 differentially methylated between different cortical areas projecting to the same targets, as well as
447 between neurons in the same areas projecting to different targets. As expected from previous
448 studies identifying IT- and ET-projecting neurons as distinct populations, these populations were
449 also the most distinct in their gene methylation. We also identified differences between both IT
450 neurons projecting to different cortical areas and between L5-ET neurons projecting to different
451 ET targets. Cortical IT neurons projecting to different cortical targets were variable in the extent
452 of their epigenetic differences. Some pairs of cortical target areas were more distinct than others

453 and these epigenetic differences were often conserved across cortical sources areas. Differences
454 between projection target pairs were typically larger than differences between cortical source areas
455 for any given pair of projection targets.
456
457 Most distinct amongst the L5-ET neurons were those projecting to the medulla. This difference
458 has been described previously for neurons in cortical area ALM[9] and we find that this difference
459 is conserved across the additional cortical areas that we analyzed, including MOp and SSp. In
460 contrast, differences between L5-ET neurons projecting to SC versus pons were more distinct in
461 some cortical areas (e.g. AI) than in others (e.g. PTLp). Dual retrograde tracer injections into both
462 SC and pons revealed a corresponding difference in the proportions of double-labeled cells in
463 different cortical areas, consistent with the expectation that neurons projecting to just one target
464 can be different while those projecting to both targets cannot.
465
466 Surprisingly, we found that a subpopulation of cortico-cortical RSP→VISp and ACA→VISp
467 neurons clustered with L5-ET cells, contrary to the expectation that L5-ET and IT cortico-cortical
468 cells are distinct populations. This suggested that some L5-ET cells might project to cortical targets
469 and this hypothesis was validated anatomically. Our anatomical experiments showed that
470 RSP→VISp cells do in fact project to many ET targets, including TH, SC and pons, and we refer
471 to this new cell type as L5 ET+CC. Although we found CC projection neurons that clustered with
472 L5-ET cells for only two of the 26 CC projections that we sampled, there remain many other
473 combinations that we did not test. It is therefore possible that future studies might reveal L5-
474 ET+CC cells projecting to cortical targets other than VISp or residing in areas other than RSP and
475 ACA.

476

477 Finally, this large-scale effort linking methylation status directly to projection targets of mouse
478 cortical neurons, allowed us to identify differences between projection cell types in TFs linked to
479 differentially methylated regions. These observations provide insight into genetic mechanisms that
480 might contribute to the differences in morphology and function of these cell types. As we have
481 illustrated, this large dataset also provides the opportunity to predict regulatory elements that might
482 be harnessed in future studies to target transgene expression to these cell types.

483

Figures

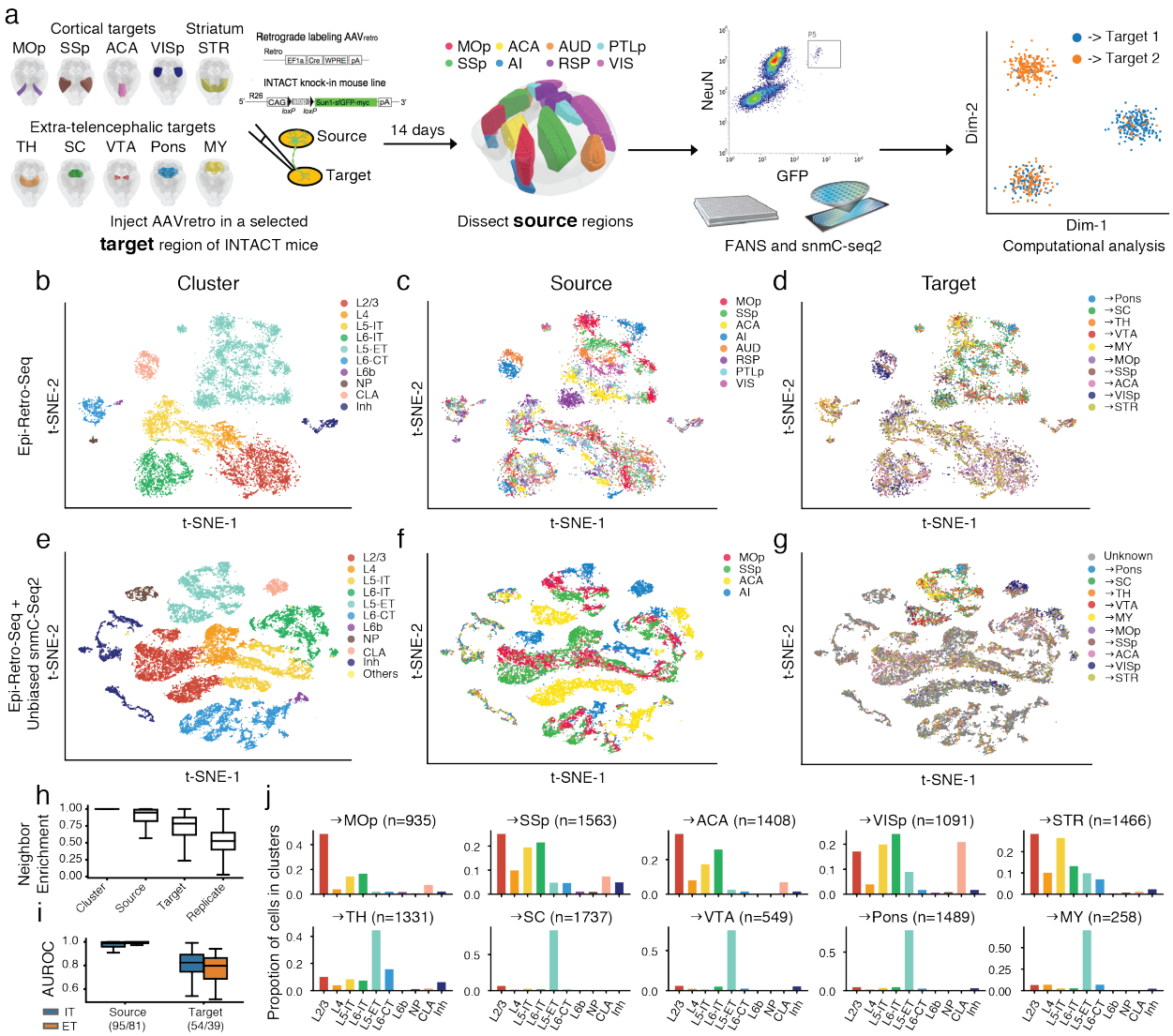

Fig. 1 The epigenomic landscape of cortical projection neurons.

a, Schematics of Epi-Retro-Seq workflow that retrogradely labels and epigenetically profiles single projection neurons. The retrograde tracer rAAV2-retro-cre was injected in one of the ten target regions (primary motor cortex (MOp), primary somatosensory cortex (SSp), anterior cingulate cortex (ACA), primary visual cortex (VISp), striatum (STR), thalamus (TH), superior colliculus (SC), the ventral tegmental area (VTA) & substantia nigra (SNr), Pons, or medulla (MY)) in INTACT knock-in mice. Therefore, nuclei of neurons that projected to the injected target

493 were labeled with cre-dependent nuclear GFP. Source regions of interest (MOp, SSp, ACA,
494 agranular insular cortex (AI), auditory cortex (AUD), retrosplenial cortex (RSP), posterior parietal
495 cortex (PTLp), or visual cortex (VIS)) were dissected 14 days after the injection, from which nuclei
496 were prepared and single $GFP^+/NeuN^+$ nuclei were isolated using fluorescence activated nuclei
497 sorting (FANS) followed by snmC-seq2 and computational analysis. Brain diagrams were derived
498 from the Allen Mouse Brain Reference Atlas (version 3 (2015)). **b-d,** Two-dimensional t-
499 distributed stochastic neighbor embedding (t-SNE) of 11,827 cortical neuron nuclei based on CH
500 methylation (mCH) levels in 100 kb genomic bins, colored by cluster (**b**), the source region of
501 neurons (**c**), or their projection target (**d**). Cortical neurons were better separated by their source
502 regions than projection targets within each major cell type cluster. **e-g**, Integrative clustering of
503 Epi-Retro-Seq and unbiased snmC-seq2 (without enrichment of projections) of neurons from
504 MOp, SSp, ACA and AI (n=21,966), colored by cluster (**e**), source region (**f**), and projection targets
505 in Epi-Retro-Seq (**g**). **h**, Neighbor enrichment scores of cells (n=11,827) categorized by cluster,
506 source, target, and replicate. **i**, AUROC of source pairs and target pairs computed for IT (blue) and
507 ET (orange) neurons based on gene body mCH. Sample sizes are shown in x-axis ticklabels. **j,** The
508 distribution across cell clusters of neurons that projected to each IT (top row) or ET (bottom row)
509 target. The elements of all boxplots are defined as: center line, median; box limits, first and third
510 quartiles; whiskers, 1.5× interquartile range.
511 IT, intra-telencephalic; ET, extra-telencephalic; NP, near-projecting; CT, corticothalamic; Inh,
512 inhibitory; CLA, claustrum; Others, cell clusters detected in unbiased snmC-seq2 but not in Epi-
513 Retro-Seq.
514

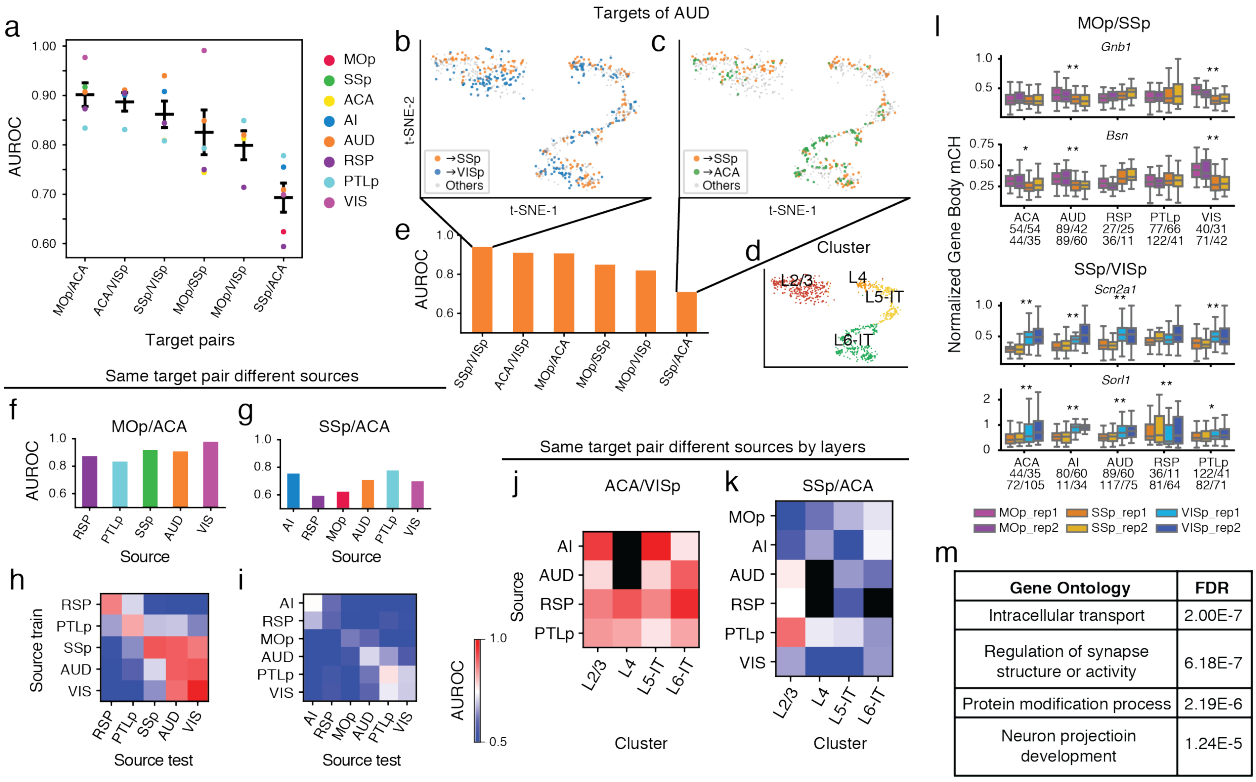

Gene Ontology	FDR
Intracellular transport	2.00E-7
Regulation of synapse structure or activity	6.18E-7
Protein modification process	2.19E-6
Neuron projectioin development	1.24E-5

Fig. 2 Epigenetic differences between IT neurons projecting to different targets.

a, AUROC from the prediction model constructed to distinguish cortical neurons projecting to one cortical target versus another was used to measure the epigenetic variation between different cortical IT neurons. A significant variation of AUROC among different projection target pairs was observed. **b-e**, Upon examining AUD IT neurons (n=737) that project to different cortical targets, AUD→SSp neurons and AUD→VISp neurons were biased toward different locations within each layer-annotated cluster (**d**) on the t-SNE plot using mCH levels in gene bodies (**b**), while AUD→SSp neurons and AUD→ACA neurons were more intermingled (**c**). The differential levels of separation on t-SNE corresponded to the high AUROC between AUD→SSp versus AUD→VISp neurons, and low AUROC between AUD→SSp versus AUD→ACA neurons (**e**). **f, g**, The AUROC for comparisons between →MOp versus →ACA neurons from different source regions varied between 0.834 and 0.977 (**f**), while the AUROC for comparisons between →SSp

versus →ACA neurons from different source regions varied between 0.594 and 0.778 (**g**), indicating overall higher levels of distinguishability between →MOp versus →ACA neurons, than between →SSp versus →ACA neurons. **h, i**, Heatmaps of AUROC from prediction models that were trained on one source region (row) and tested on another source region (column) to distinguish between neurons projecting to →MOp versus →ACA (**h**), or between →SSp versus →ACA neurons (**i**). **j, k**, Heatmaps of AUROC from prediction models that were trained and tested on neurons from each cortical layer (column) in each source region (row), to distinguish between →ACA versus →VISp neurons (**j**), or between →SSp versus →ACA neurons (**k**). **l**, Boxplots of example genes that were differentially methylated at CH sites (CH-DMGs) between →MOp versus →SSp neurons (top), or between →SSp versus →VISp neurons (bottom). The sample sizes are shown as ticklabels of x-axis. ** represents false discovery rate (FDR)<0.01 and * represents FDR<0.1. **m**, Gene ontology (GO) enrichment of 1,830 CH-DMGs between cortical neurons projecting to different cortical targets. The elements of all boxplots are defined as: center line, median; box limits, first and third quartiles; whiskers, 1.5× interquartile range. Center lines and error bars in (a) represent the means and standard errors of the means.

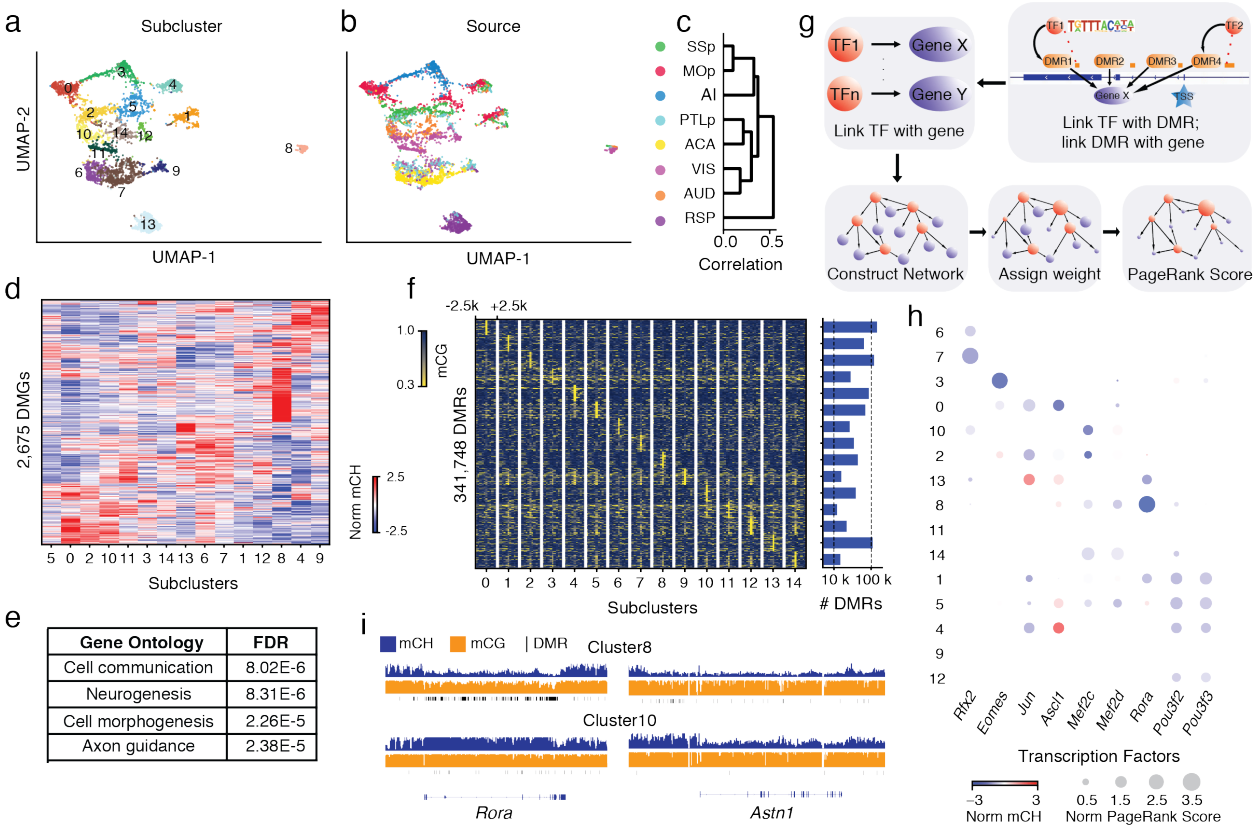

Fig. 3 Epigenetic diversity of L5-ET neurons.

a, b, Fifteen subclusters of L5-ET neurons (n=4,176) were identified and visualized on the uniform manifold approximation and projection (UMAP) plot generated using mCH levels in 100 kb genomic bins, colored by cluster (**a**), or the source region of neurons (**b**). **c**, Dendrogram shows the similarities between mCH profiles of L5-ET neurons from different source regions. **d, e**, In total, 2,675 CH-DMGs were identified in pairwise comparisons between L5-ET subclusters. Gene body mCH levels in each subcluster were visualized in the heatmap (**d**). Gene ontology (GO) enrichment of the CH-DMGs (**e**). **f**, Analysis of CG methylation (mCG) identified 341,748 differentially methylated regions (CG-DMRs) across the 15 L5-ET subclusters. The mCG levels at CG-DMRs and their 5kb flanking genomic regions in each subcluster were visualized in the heatmap (left). The numbers of CG-DMRs hypo-methylated in each subcluster were plotted in the bar chart (right). **g**, Workflow of the PageRank algorithm to infer crucial transcription factors. **h**,

557 Examples of some predicted key regulator TFs are shown in the bubble plot. The size of each dot
558 represents the normalized PageRank score of the TF. The color of the dot represents the gene body
559 mCH of the TF in the corresponding L5-ET subcluster. **i**, Browser tracks of mCH (blue), mCG
560 (orange), and CG-DMRs (black ticks) at *Rora* and its predicted gene target *Astn1*.
561

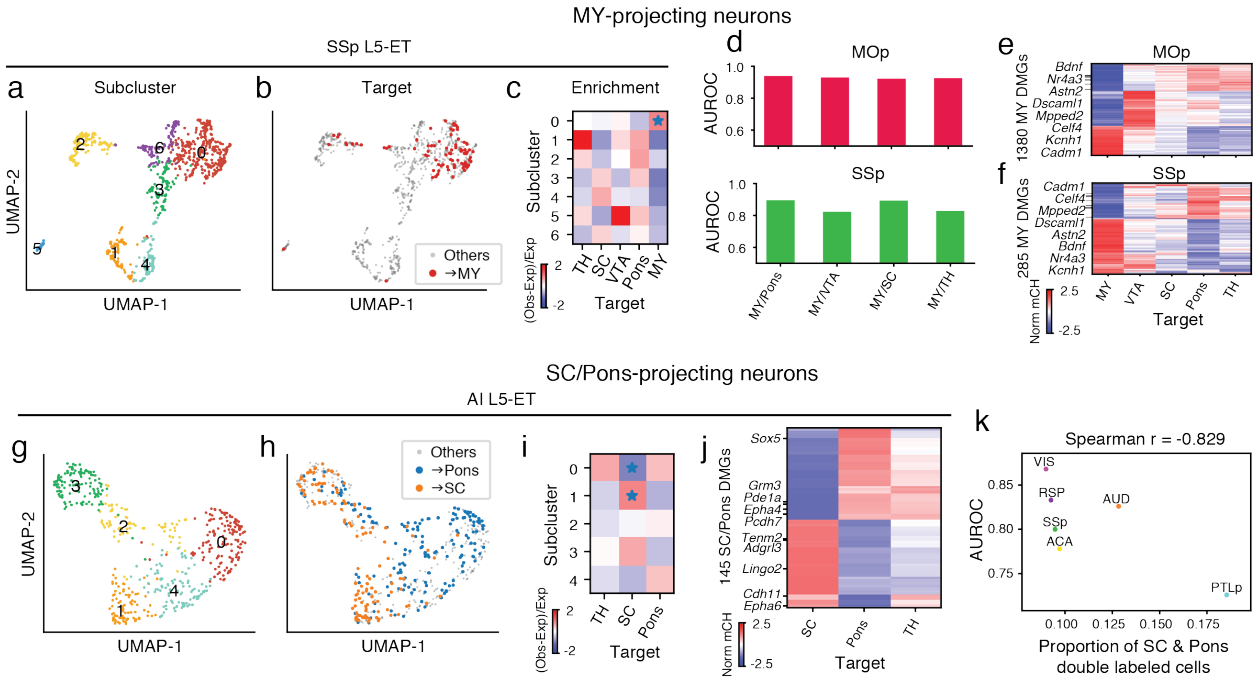

Fig. 4 Epigenetic differences between L5-ET neurons projecting to different targets. **a-f**, L5-ET neurons projecting to MY had more distinct DNA methylation profiles than other L5-ET neurons: SSp L5-ET neurons (n=884) segregated into 7 subclusters as visualized on the UMAP plot generated using mCH levels in 100 kb genomic bins (**a**). Compared to other SSp L5-ET neurons, SSp→MY neurons occupied a distinct space on the UMAP that corresponded to SSp subcluster 0 (**b**). The enrichment of SSp→MY neurons in SSp subclusters was calculated and visualized in the heatmap (**c**; * represents FDR<0.05). We constructed prediction models to distinguish →MY neurons from →Pons, →VTA, →SC, and →TH neurons. AUROC scores showed that the models performed well in both MOp (**d**, top) and SSp (**d**, bottom) for comparisons between →MY neurons versus neurons projecting to each of the other targets. **e, f**, In total 1,380 CH-DMGs were identified in pairwise comparisons between MOp→MY neurons and MOp neurons projecting to another subcortical ET target. The gene body mCH levels of these CH-DMGs in MOp neurons projecting to each ET target were visualized in the heatmap (**e**). Similarly,

285 SSp→MY CH-DMGs were identified and plotted in the heatmap (**f**). Gene names for example CH-DMGs that were hypo-methylated in both MOp→MY and SSp→MY neurons are highlighted in the heatmaps (**e, f**). **g-k**, Epigenetic differences between Pons-projecting versus SC-projecting neurons varied across cortical regions: In AI, L5-ET neurons (n=531) separated into 5 subclusters as visualized on the UMAP plot (**g**). AI→Pons and AI→SC neurons occupied different positions on the UMAP (**h**), corresponding to their differential enrichment in AI subclusters 0 and 1 (**i**; * indicating FDR<0.05). 145 CH-DMGs were identified between AI→SC versus AI→Pons neurons. mCH levels of these SC/Pons CH-DMGs in AI→SC, →Pons, and →TH neurons were plotted in the heatmap (**j**). **k**, The variation of AUROC from prediction models to distinguish →SC versus →Pons neurons from different source regions suggested that the levels of distinction between →SC and →Pons neurons vary between cortical regions. From this observation, we hypothesized that different cortical regions had different proportions of neurons that made dual projections to both SC and Pons. The proportion of double labeled cells was negatively correlated with the AUROC score in each source area, supporting the hypothesis.

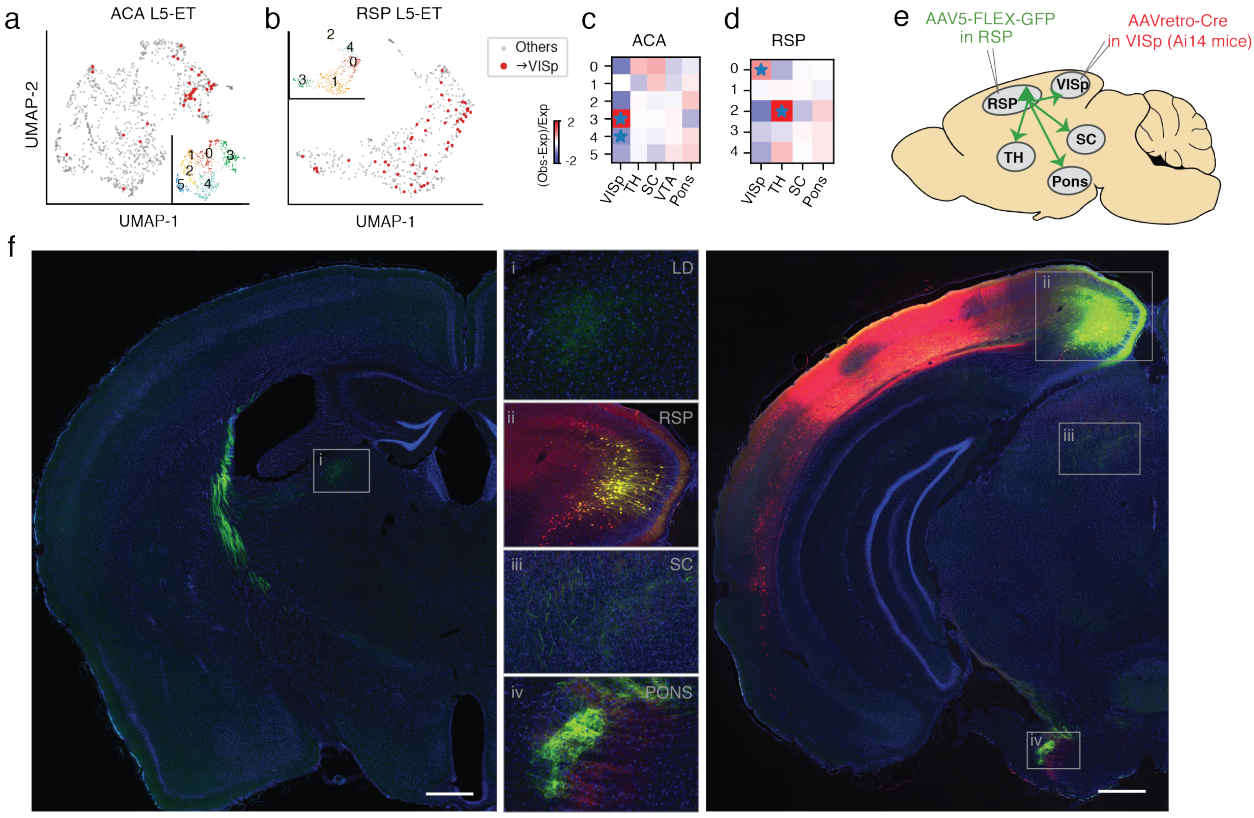

Fig. 5 A L5-ET neuron type that projects to both ET and cortical targets (L5-ET+CC). **a**, UMAP embedding of ACA L5-ET neurons (n=1,131) using mCH in 100 kb bins, colored by projection targets (ACA→VISp in red, n=36) and subclusters (Inset). **b**, UMAP embedding of RSP L5-ET neurons (n=516) using mCH in 100 kb bins, colored by projection targets (RSP→VISp in red, n=53) and subclusters (Inset). **c-d**, ACA→VISp neurons were enriched in ACA L5-ET subcluster 3 and depleted from subcluster 4 (**c**). RSP→VISp neurons were enriched in RSP L5-ET subcluster 0 (**d**). (* indicating FDR<0.05). These observations suggested that some ACA and RSP neurons project to both ET and cortical targets (L5-ET+CC). To validate the existence of this previously undescribed L5-ET+CC cell type, we designed an anatomical labeling experiment as illustrated in **e**. AAVretro-Cre was injected into VISp of Ai14 (Cre-dependent TdTomato) mice, and AAV5-FLEX-GFP (Cre-dependent GFP) was injected in RSP. Therefore, RSP→VISp neurons, including their axonal projections, were selectively labeled with GFP. If RSP→VISp

604 neurons also project to ET targets (L5-ET+CC neurons exist), GFP-labeled axons would be
605 expected in subcortical ET targets such as SC, Pons, and TH. **f**, We performed these labeling
606 experiments in three Ai14 mice and observed the same result in all mice. Examples of brain
607 sections from one animal are shown. VISp neurons at the AAVretro-Cre injection site were labeled
608 by tdTomato (red). RSP→VISp neurons were labeled with GFP (green), among which
609 RSP→VISp neurons at the AAV5-FLEX-GFP injection site were labeled with both tdTomato and
610 GFP (yellow; inset ii). Strong GFP signals of RSP→VISp axon terminals in subcortical ET regions
611 were observed, including in the laterodorsal (LD) nucleus of the thalamus (inset i), SC (inset iii),
612 and Pons (inset iv). Scale bars: 500 μm (low magnification).
613

614 **Methods**

615 **Experimental Animals.**

616 All experimental procedures using live animals were approved by the Salk Institute Animal Care
617 and Use Committee. The knock-in mouse line, R26R-CAG-loxp-stop-loxp-Sun1-sfGFP-Myc
618 (INTACT) was used for most experiments[4] and they were maintained on a C57BL/6J background.
619 42-49 day old adult male and female INTACT mice were used for the retrograde labeling
620 experiment. Adult C57BL/6J "wild-type" mice were used for double-retrograde labeling
621 experiments.

622

623 **Surgical Procedures for Viral Vector and Tracer Injections.**

624 To label neurons projecting to regions of interest, injections of rAAV2-retro-Cre (produced by
625 Salk Vector Core or Vigene, $2x10^{12}$ to $1x10^{13}$ viral genomes/ml, produced with capsid from
626 Addgene plasmid #81070 packaging pAAV-EF1a-Cre from Addgene plasmid #55636) were made
627 into both hemispheres of the INTACT mice. Animals were anesthetized with either
628 ketamine/xylazine or isoflurane, placed in a stereotaxic frame, and 0.1 to 0.5 microliters of AAV
629 was injected by pressure into stereotaxic coordinates corresponding to the desired projection target.
630 A list of injection coordinates and volumes is provided in Supplementary Table 1. At least 2 male
631 and 2 female mice were injected for each projection target. To label RSP neurons that project to
632 VISp, RSP was injected with rAAV2-retro-Cre and VISp was injected with AAV-FLEX-GFP
633 (Salk Vector Core) in each of 3 adult, Ai14 mice.

634

635 **Assessment of Double-Retrograde Labeling.**

636 To assess double-labeling of cortical cells projecting to Pons and/or Superior Colliculus,
637 stereotaxic pressure injections of 0.1-0.2 microliters of 0.25-0.5% of Cholera Toxin Subunit B
638 (CTB), Alexa Fluor 488 or 647 conjugated (Molecular Probes), were made into the pons and into
639 SC of 4 mice. 6-7 days later, animals were perfused with phosphate buffered saline (PBS) followed
640 by 4% paraformaldehyde in PBS. Brains were removed and sectioned coronally at 40 microns
641 thickness with a freezing microtome. Sections were mounted and imaged with a 20X
642 epifluorescence objective and images assessed to identify single and double-labeled neurons that
643 were assigned to cortical areas. Only neurons in regions where labeled cells from both injections
644 overlapped were counted. Therefore, some cortical areas in which there was no overlap are not
645 included. For each animal, double labeled cells were quantified for each region as the proportion
646 of double-labeled divided by the sum of all labeled cells. Mean values from the 4 animals are
647 plotted in Fig. 4k.

648

649 **Brain dissection.**

650 Approximately two weeks after the AAVretro injection, brains were extracted from the 56-63 day
651 old INTACT mice, immediately submerged in ice-cold slicing buffer (2.5mM KCl, 0.5mM $CaCl_2$,
652 7mM $MgCl_2$, 1.25mM NaH_2PO4, 110mM sucrose, 10mM glucose and 25mM $NaHCO_3$) that was
653 bubbled with carbogen, and sliced into 0.6 mm coronal sections starting from the frontal pole.
654 From each AAVretro-injected brain, the slices were kept in the ice-cold dissection buffer from
655 which selected brain regions (Supplementary Table 1) were manually dissected under a fluorescent
656 dissecting microscope (Olympus SZX16), following the Allen Mouse Common Coordinate

657 Framework (CCF), Reference Atlas, Version 3 (2015) (Extended Data Fig. 1). The dissected brain
658 tissues were transferred to prelabeled microcentrifuge tubes, immediately frozen in dry ice, and
659 subsequently stored at -80ºC.
660
661 **Nuclei preparation and single-nucleus isolation.**
662 For each dissected brain region, samples from 2 males and 2 females were pooled separately as
663 biological replicates for nuclei preparation. The 2-mL glass tissue dounce homogenizer and pestles
664 (Sigma-Aldrich D8938-1SET) were pre-chilled on ice. Nuclei were prepared using a modified
665 protocol as reported by Lacar et al., 2016[22]. In summary, the frozen brain tissues were transferred
666 to the dounce homogenizer with 1 mL ice-cold NIM buffer (0.25M sucrose, 25mM KCl, 5mM
667 $MgCl_2$, 10mM Tris-HCl (pH7.4), 1mM DTT (Sigma 646563), 10µl of protease inhibitor (Sigma
668 P8340)), with 0.1% Triton X-100 and 5µM Hoechst 33342 (Invitrogen H3570), and gently
669 homogenized on ice with the pestle 10-15 times. The homogenate was transferred to pre-chilled
670 microcentrifuge tubes and centrifuged at 1000 rcf for 8 min at 4ºC to pellet the nuclei. The pellet
671 was resuspended in 1 mL ice-cold NIM buffer, and again centrifuged at 1000 rcf for 8 min at 4ºC.
672 The pellet was then resuspended in 450 µL of ice-cold NSB buffer (0.25M sucrose, 5mM $MgCl_2$,
673 10mM Tris-HCl (pH7.4), 1mM DTT, 9ul of Protease inhibitor), and filtered through 40µM cell
674 strainer. The filtered nuclei suspension was incubated on ice for at least 30 minutes with 50µl of
675 nuclease-free BSA for at least 10 minutes, then incubated with GFP antibody, Alexa Fluor 488
676 (Invitrogen, A-21311) and anti-NeuN antibody (EMD Millipore MAB377) conjugated with Alexa
677 Fluor 647 (Invitrogen A20173). $GFP^+/NeuN^+$ single nuclei were isolated using fluorescence-
678 activated nuclei sorting (FANS) on a BD Influx sorter with 100µm nozzle, and sorted into 384-
679 well plates preloaded with 2µl of digestion buffer for snmC-seq2[15] (20 mL digestion buffer consists

680 of 10 mL M-digestion buffer (2×, Zymo D5021-9), 1 ml Proteinase K (20 mg, Zymo D3001-2-20),
681 9 mL water, and 10 µL unmethylated lambda DNA (100 pg/µL, Promega, D1521)). The collected
682 plates were incubated at 50ºC for 20 minutes then stored at -20 ºC.
683
684 **snmC-Seq2 library preparation.**
685 The bisulfite conversion and library preparation were performed following the detailed snmC-seq2
686 protocol as previously described[15]. The snmC-Seq2 libraries were sequenced on Illumina Novaseq
687 6000 using the S4 flow cell 2 x 150 bp mode.
688
689 **Reads processing and quality controls.**
690 We used the cemba-data pipeline to generate allc files from fastq files (cemba-data.rtfd.io), as
691 described in Luo et al[6]. Specifically, the fastq files were first demultiplexed into single cells and
692 trimmed of Illumina adaptors and 10 bp on both sides with Cutadapt[23]. The reads were mapped to
693 mm10 INTACT mouse genome using Bismark[24] with Bowtie2 aligner for each single end
694 separately. The reads with MAPQ smaller than 10 were excluded. Potential PCR duplicates were
695 removed with Picard MarkDuplicates. The reads from two ends were then merged to generate allc
696 files using call_methylated_sites function in methylpy[25]. The global mCCC level was used to
697 estimate the non-conversion rate of bisulfite treatment. The cells with less than 500 k non-clonal
698 reads or non-conversion rate greater than 1% were removed from further analysis.
699

700 **Methylation data processing.**

701 For each single cell, we computed the methylated CH (mc) and total CH (tc) basecalls of all 100
702 kb bins across the genome and all gene bodies annotated in GENCODE vM10[26]. The autosomal
703 bins that were covered by more than 100 basecalls in greater than 95% of cells were used for
704 further analysis. The autosomal genes that were covered by more than 100 basecalls in greater than
705 80% of cells were used for further analysis.

706

707 **Computing posterior methylation levels.**

708 For each cell, we calculated the mean (m) and variance (v) of the mCH level across the 100 kb
709 bins or genes. Then a beta distribution was fit for each cell i, where the parameters were then
710 estimated by

711 $$\alpha_i = m_i(\frac{m_i(1-m_i)}{v_i} - 1)$$

712 $$\beta_i = (1-m_i)(\frac{m_i(1-m_i)}{v_i} - 1)$$

713 We then calculated the posterior mCH of each bin by

714 $$ratio_{ij} = \frac{\alpha_i + mc_{ij}}{\alpha_i + \beta_i + tc_{ij}}$$

715 We normalized this rate by the cell's global mean methylation by

716 $$global_i = \frac{\alpha_i}{\alpha_i + \beta_i}$$

717 $$M_{ij} = \frac{ratio_{ij}}{global_i}$$

718 The values greater than 10 in M were set to 10. After normalization, M_{ij} is close to 1 when tc_{ij} is
719 close to 0.
720
721 **Identification of highly variable bins.**
722 Highly variable methylation features were selected based on a modified version of the
723 highly_variable_genes function in Scanpy[27]. In brief, since both the mean methylation level and
724 the mean coverage of a feature (100 kb bin or gene) can impact methylation level dispersion[6], we
725 grouped features that fall into a combined bin of mean and coverage, and then normalized the
726 dispersion within each group. After dispersion normalization, we selected the top 2,000 features
727 based on normalized dispersion for dimension reduction.
728
729 **Removing potential doublets.**
730 By plotting all cells on t-SNE, we noticed a cell population that was located in the center of the
731 plot and has a greater number of non-clonal reads than the others. To remove these potential
732 doublets, we modified scrublet[28] to adopt it to methylation data. Specifically, we first simulate the
733 doublet cells by randomly selecting two cells in our dataset and sum the methylation/total basecalls
734 of the two cells. Then the methylation levels of the simulated cells were computed using the
735 posterior computing method. We simulated twice the number of doublets as the number of real
736 cells. The top 2,000 highly variable features were selected for dimension reduction with principal
737 component analysis (PCA) and the top 50 PCs were used to train a k-nearest neighbor (kNN)
738 classifier (k=50) to predict a doublet score for each cell. Based on the histogram of doublet scores

739 of real and simulated doublet cells, the cells with doublet score higher than 0.1 were removed from
740 further analysis. After removing the potential doublets, 13,414 cells were kept for further analysis.
741
742 **Cell clustering and annotation.**
743 After removing potential doublets, the top 2,000 highly variable features were selected for
744 dimension reduction with PCA. The top 50 PCs were used for t-SNE visualization and construction
745 of kNN graph (G) with Euclidean distance (k=25). We use A to represent the connectivity of G,
746 where A_{ij} is 1 if node j is among the 25 nearest neighbors of node i, otherwise 0. The edge weights
747 of G were assigned as the jaccard distance of the connectivity matrix A. We ran Louvain clustering
748 (https://github.com/taynaud/python-louvain) with resolution 1.2 to partition the cells into 31
749 clusters and merged these clusters into major cell types based on known marker genes. The 11,827
750 cells within neuronal cell clusters were selected for further analysis.
751
752 **Neighbor enrichment score.**
753 The score was used to quantify the enrichment of cells that belong to the same category among the
754 neighbors of each cell. A higher score represents the cells are more likely to form clusters with the
755 cells belonging to the same category rather than in the other categories. The advantage of this score
756 is that it only considers the local effect so that would remain high if the cells in a category form
757 several different clusters that dissimilar with each other. The score was computed as follows.
758 Euclidean distances between each pair of cells were computed using the first 50 PCs. For each cell,
759 we found its 25 nearest neighbors in the same category, and $25r$ nearest neighbors from other

760 categories, where r is the ratio between total number of cells in other categories and total number
761 of cells in the same category. The area under the receiver operating characteristic (AUROC) using
762 distances between the cell and these neighbor cells for distinguishing the categories were defined
763 as the neighbor enrichment score of this cell. The methylation pattern of male and female mice are
764 highly similar on autosome; therefore, the two genders were treated as replicates in the analyses.
765
766 **Pairwise prediction of the source and target regions.**
767 Based on the sources, and targets, the neurons could be separated into groups. Each group contains
768 the neurons projecting from a specific source to a specific target. To test the similarity of two
769 groups of cells based on DNA methylation, we trained logistic regression models to predict the
770 group label of each cell. The posterior of 100 kb-bin or gene body mCH were used as features. We
771 split the cells into training and testing sets based on the gender of the mice where the cell came
772 from. The area under the receiver operating characteristic (AUROC) from cross-validation was
773 used to measure the performance of the model. The higher AUROC represents better ability of the
774 model to present the group label, which indicated the two groups had larger mCH differences and
775 were more distinguishable.
776 When the groups being studied contained cells from different clusters (e.g. cortical projecting
777 neurons in one source), we up-sampled the training set to make it better capture the group
778 differences rather than the differences of cell distributions across clusters. For example, when
779 comparing neurons projecting to two different cortical targets, the cluster composition differences
780 could make the model over-weight the features marking different clusters. To get rid of this bias,
781 we randomly repeated the neurons from the under-representing group and ensured the two groups

782 had the sample number of training samples in each cluster. The models were then trained and
783 tested in the same setting as mentioned above.
784 Several reasons could contribute to a low prediction performance. 1) Some neurons make
785 projections to several targets simultaneously. These could result in the neurons being captured by
786 multiple retrograde labeling experiments of different targets. It would be impossible to predict a
787 single label with our pairwise models for this type of neuron. 2) Some neurons project to different
788 target regions but have tiny epigenetic differences. 3) The epigenetic differences between neurons
789 projecting to different targets varies across replicates. In this study, male and female mice were
790 treated as biological replicates after removing sex chromosomes. Although methylation patterns
791 of autosomes are similar, differences between genders might still exist. 4) The contamination
792 levels of some projections are high, which make larger noise and hinder the models to capture real
793 signals. 5) The sample sizes of some projections are small, which make the learning more
794 challenging.
795 If the cross source/cluster predictions (described below) performed better than the within
796 source/cluster models, we would suspect that shared differences between neurons projecting to
797 different targets exist across sources/clusters, and the major reason for lower accuracies of within
798 source/cluster models might be 4) or 5) described above. To systematically distinguish 1) to 3),
799 other anatomic and genetic validation are still needed.
800
801 **Cross source prediction.**
802 The logistic regression models were trained to predict the projection targets in one source and
803 tested in the other source. The training set and testing set came from mice of different genders.

804 Specifically, the final AUROC were the average of AUROCs by training in male mice and testing
805 in female mice and by training in female mice and testing in male mice. For cortical targets, we
806 up-sampled the training set in the same way as the above section.
807
808 **Cross cluster prediction.**
809 This analysis was specifically for CC projection neurons to study whether the mCH differences
810 between projection neurons were shared or distinct across clusters (layers). The logistic regression
811 models were trained to predict the projection targets in one cluster and tested in the other cluster.
812 The training set and testing set came from mice of different genders.
813
814 **Identification of differentially CH-methylated genes (CH-DMGs).**
815 Wilcoxon rank-sum test and t test were widely used to identify differential genes in single-cell
816 studies[27], which consider each cell as an independent sample. However, the cells from the same
817 replicate, individual, or batch would be more similar than the cells from different ones. Therefore,
818 considering all cells as independent samples would overestimate the statistical power in single-
819 cell data. To address this problem and take the replicate-level variation into consideration, we used
820 a linear mixed model for the differential analysis and performed paired-wise comparisons between
821 groups. The posterior mCH level of 12,261 autosomal genes after coverage filters were used for
822 these analyses. The posterior gene-body mCH was used as dependent variables. Each individual
823 mouse was considered as a random effect. The global mCH levels and the gender of the mice were
824 considered as fixed effects. Other fixed effects were determined based on the comparison.
825 Specifically,

826 For DMGs between L5-ET clusters:

827 Gene_mCH ~ cluster + gender + global_mCH + (1 | mouse)

828 For DMGs between cortical targets in each source:

829 Gene_mCH ~ target + cluster + gender + global_mCH + (1 | mouse)

830 For DMGs between ET targets in each source:

831 Gene_mCH ~ target + gender + global_mCH + (1 | mouse)

832 Each gene was tested separately, and two-sided Wald test was performed to estimate the *P* value
833 for the effect being tested. FDR was computed for each pair of groups with the
834 Benjamini/Hochberg process. The fold-change of each gene was computed by the average mCH
835 across cells in one group divided by the average mCH across cells in the other group, with pseudo-
836 counts of 0.1. The criterions for significance when testing difference variables were distinct and
837 shown as follows. For DMGs between L5-ET clusters: absolute log fold-change greater than log1.5
838 and FDR smaller than 0.01. For DMGs between IT targets or between ET targets in each source:
839 absolute log fold-change greater than log 1.25 and FDR smaller than 0.01.

840

841 **Identification of differentially CG-methylated regions (CG-DMRs).**

842 To identify DMRs, we merged the allc files of individual cells assigned to the same cluster to
843 create a pseudo-bulk allc table for each cluster. Then we selected all the CG sites and combined
844 the methylation on two DNA strands for each CpG site. We run methylpy[25] DMRfind to identify
845 the DMRs and require the DMRs to contain at least 2 differentially methylated CpG sites (DMS).

846

847 **Inference of crucial transcription factors (TF) with PageRank.**

848 The method was modified from Taiji[19] to integrate the information of both gene body and
849 regulatory regions. The 537 motifs in JASPAR 2018 non-redundant core vertebrate database[29]
850 were used for these analyses. We scanned each of the motifs against the mm10 INTACT mouse
851 genome with ame[30] and *P* value cutoff as 1e-4. The DMRs between clusters were expanded 100
852 bp on both sides, and the ones overlapping with motifs were assigned to the corresponding TF.
853 The DMRs were also assigned to the potential genes they regulated using GREAT[31]. The TFs were
854 then linked with the target genes based on these DMRs that links to both the upstream TFs and the
855 downstream genes. A gene regulation network was constructed where the nodes represented the
856 genes and edges represented the links between TF genes and target genes.

857 To assign weights to the edges and initiate the node importance, the normalized $n_{cluster} \times n_{gene}$
858 methylation matrix (M) were min-max normalized across clusters to 0-1 by

859 $$N_{ij} = \frac{M_{ij} - min_{0<j'\leq n_{gene}} M_{ij'}}{max_{0<j'\leq n_{gene}} M_{ij'} - min_{0<j'\leq n_{gene}} M_{ij'}}$$

860 , and $1 - N_i$ were used as the predicted expression of each gene in cluster i. The predicted
861 expressions of all genes were used as starting importance I_0. Then we used a $n_{gene} \times n_{gene}$ matrix
862 A to represent the adjacency matrix of TF-gene regulation network, where A_{ij} was assigned as the
863 predicted expression level of gene i if gene i is a TF. To ensure an undirected propagation, we
864 used $B = A + A^T$ as the final adjacency matrix. B was normalized by row into the transition
865 matrix P by

866 $$P_{ij} = \frac{B_{ij}}{\sum_{j'=1}^{n_{gene}} B_{ij'}}$$

867 Next we performed a diffusion step of the PageRank scores through the network. For iteration t,
868 the PageRank scores were computed by

869 $$I_t = P \times I_{t-1} + rp \times I_0$$

870 , where rp represents a restart probability to balance the global and local effect of the propagation
871 on the network. The diffusion step was stopped when $|I_t - I_t| < 10^{-5}$.

872

873 **Clustering of L5-ET cells in each source region.**

874 L5-ET neurons from Epi-Retro-Seq and unbiased snmC-Seq were combined in this analysis. After
875 the same process as clustering all cells to derive posterior mCH level and select highly variable
876 features, the first 30 PCs were used for computing kNN (k=15) and Louvain clustering. The
877 resolutions used for source regions were 1.6 for MOp, AI, AUD, and RSP; 2.0 for SSp and PTLp;
878 1.0 for VISp; and 2.5 for ACA. The resolutions were determined based on visually examining the
879 cluster numbers and projection enrichment.

880 To confirm that there were epigenetic features distinguishing the clusters, we computed the
881 differentially methylated 100 kb bins (DMBs) across all pairs of subclusters using two-sided
882 Wilcoxon rank-sum test. The bins were defined as differential if the absolute log fold-change
883 between subclusters were greater than log 1.5, and FDR of the test smaller than 0.01. We also used
884 AUROC>0.85 and AUPR>0.6 to define DMBs, which provided similar results. Two subclusters
885 in RSP that had less than 5 DMBs were merged.

886

887 **Tests of projection enrichment in subclusters.**

888 As described above, the cells from the same replicate would be more similar, and considering all
889 cells as independent samples will overestimate the statistical power in single-cell data. Therefore,
890 we used linear mixed models to test for significant enrichment of particular projections in each
891 subcluster, considering the mouse where the cells came from. The subclsuter was used as
892 dependent variables. Each individual mouse was considered as a random effect. The projection
893 target was considered as fixed effects. [Subcluster ~ Target + (1 | mouse)]

894 Each projection target and each cluster were tested separately, and two-sided Wald test was
895 performed to estimate the *P* value for the effect being tested. FDR was computed for each source
896 with the Benjamini/Hochberg process. (Obs-Exp)/Exp in the enrichment matrices were computed
897 using the same method as in Pearson's chi-square test.

898

899 **Integration of Epi-Retro-Seq and Retro-Seq.**

900 Single-cell transcriptomic data from Tasic 2018[9,13] was downloaded from NCBI Gene Expression
901 Omnibus (GSE115746). 365 cells within clusters of 'L5 PT ALM *Npsr1*', 'L5 PT ALM *Slco2a1*',
902 and 'L5 PT ALM *Hpgd*' were selected for integration analysis. The raw data was preprocessed
903 using Scanpy[27]. Specifically, the read counts were normalized by the total read counts per cell and
904 log transformed. Top 10,000 highly variable genes were identified and z-score scaled across all
905 the cells. For methylation data, the posterior methylation levels of 12,261 genes in the 4,176 L5-
906 ET cells were z-score scaled across all the cells and used for integration. We used Scanorama[32] to
907 integrate the z-scored expression matrix and minus z-scored methylation matrix with sigma equal
908 to 100.

Overlap score.

Overlap score quantifies the similarity of the distributions of two groups of cells across clusters, where higher scores represent the two groups are more likely to be co-clustered. The scores were computed using the same method as in Hodge et al[14]. Specifically, a $n_{group} \times n_{cluster}$ matrix C was first computed, where C_{ik} represents the number of group i cells in cluster k. C was normalized by row to D, and the overlap score between group i and group j was defined as $\sum_{k=1}^{n_{cluster}} min(D_{ik}, D_{jk})$.

Data access and code availability

The data can be accessed via the NeMO ftp archive: http://data.nemoarchive.org/biccn/lab/callaway/projection/sncell/**.** The code for all of the analyses and the link to data browser can be found at https://github.com/zhoujt1994/Zhou2019.git

Author contribution

Contribution to research design: E.M.C., Z.Z, M.M.B., J.R.E., J.Z., X.J., K.L.

Contribution to data collection: Z.Z., Y.P., A.R., E.W., C.L., M.A.K., A.F., P.A.M, A.B, A.A., M.V., L.B., C.F., J.R.N., R.G.C., M.R., M.J., T.I., B.D., J.B.S, C.O., M.M.B.

Contribution to data analysis: J.Z., P.T, Z.Z., E.M.C, M.A.K, A.F., H.L., S.N.

Contribution to data archive/infrastructure: E.A.M., Z.Z., Y.P., A.R., A.B.

929 Contribution to research coordination: Z.Z., E.M.C., J.R.E., M.M.B., Y.P., X.J., E.W., C.L.,
930 E.A.M., K.L.
931 Contribution to writing manuscript: J.Z., Z.Z., E.M.C., P.T., J.R.E., E.A.M., M.M.B.
932

933 **Acknowledgements**

934 We thank Dr. Kai Zhang for advice on the PageRank algorithm, and Dr. Jesse R. Dixon for
935 insightful comments. We are grateful to Dr. Michael Nunn for help with management of the project.
936 This work is supported by NIMH U19MH114831 to E.M.C and J.R.E. M.A.K. is supported by
937 NEI F31 EY028853. The Flow Cytometry Core Facility of the Salk Institute is supported by
938 funding from NIH-NCI CCSG: P30 014195. J.R.E is an investigator of the Howard Hughes
939 Medical Institute.
940

941 **References**

942 1. Luo, L., Callaway, E. M. & Svoboda, K. Genetic dissection of neural circuits. *Neuron* **57**,
943 634–660 (2008).
944 2. Luo, L., Callaway, E. M. & Svoboda, K. Genetic Dissection of Neural Circuits: A Decade
945 of Progress. *Neuron* **98**, 256–281 (2018).
946 3. Mukamel, E. A. & Ngai, J. Perspectives on defining cell types in the brain. *Curr. Opin.*
947 *Neurobiol.* **56**, 61–68 (2019).
948 4. Mo, A. *et al.* Epigenomic Signatures of Neuronal Diversity in the Mammalian Brain.
949 *Neuron* **86**, 1369–1384 (2015).
950 5. Luo, C. *et al.* Single-cell methylomes identify neuronal subtypes and regulatory elements in

951 mammalian cortex. *Science* **357**, 600–604 (2017).

952 6. Luo, C. *et al.* Single nucleus multi-omics links human cortical cell regulatory genome
953 diversity to disease risk variants. *bioRxiv* 2019.12.11.873398 (2019)
954 doi:10.1101/2019.12.11.873398.

955 7. Lister, R. *et al.* Global epigenomic reconfiguration during mammalian brain development.
956 *Science* **341**, 1237905 (2013).

957 8. Price, A. J. *et al.* Divergent neuronal DNA methylation patterns across human cortical
958 development reveal critical periods and a unique role of CpH methylation. *Genome Biol.* **20**,
959 196 (2019).

960 9. Economo, M. N. *et al.* Distinct descending motor cortex pathways and their roles in
961 movement. *Nature* **563**, 79–84 (2018).

962 10. Chen, X. *et al.* High-Throughput Mapping of Long-Range Neuronal Projection Using In
963 Situ Sequencing. *Cell* **179**, 772–786.e19 (2019).

964 11. Klingler, E., Prados, J., Kebschull, J. M., Dayer, A. & Zador, A. M. Single-cell molecular
965 connectomics of intracortically-projecting neurons. *BioRxIV* (2018).

966 12. Kim, D.-W. *et al.* Multimodal Analysis of Cell Types in a Hypothalamic Node Controlling
967 Social Behavior. *Cell* **179**, 713–728.e17 (2019).

968 13. Tasic, B. *et al.* Shared and distinct transcriptomic cell types across neocortical areas. *Nature*
969 **563**, 72–78 (2018).

970 14. Hodge, R. D. *et al.* Conserved cell types with divergent features in human versus mouse
971 cortex. *Nature* **573**, 61–68 (2019).

972 15. Luo, C. *et al.* Robust single-cell DNA methylome profiling with snmC-seq2. *Nat. Commun.*
973 **9**, 3824 (2018).

974 16. Fejtova, A. *et al.* Dynein light chain regulates axonal trafficking and synaptic levels of
975 Bassoon. *J. Cell Biol.* **185**, 341–355 (2009).
976 17. Sanders, S. J. *et al.* Progress in Understanding and Treating SCN2A-Mediated Disorders.
977 *Trends Neurosci.* **41**, 442–456 (2018).
978 18. Zingg, B. *et al.* Neural networks of the mouse neocortex. *Cell* **156**, 1096–1111 (2014).
979 19. Zhang, K., Wang, M., Zhao, Y. & Wang, W. Taiji: System-level identification of key
980 transcription factors reveals transcriptional waves in mouse embryonic development. *Sci*
981 *Adv* **5**, eaav3262 (2019).
982 20. Fries, W., Keizer, K. & Kuypers, H. G. Large layer VI cells in macaque striate cortex
983 (Meynert cells) project to both superior colliculus and prestriate visual area V5. *Exp. Brain*
984 *Res.* **58**, 613–616 (1985).
985 21. vogt Weisenhorn, D. M., Illing, R. B. & Spatz, W. B. Morphology and connections of
986 neurons in area 17 projecting to the extrastriate areas MT and 19DM and to the superior
987 colliculus in the monkey Callithrix jacchus. *J. Comp. Neurol.* **362**, 233–255 (1995).
988 22. Lacar, B. *et al.* Nuclear RNA-seq of single neurons reveals molecular signatures of
989 activation. *Nat. Commun.* **7**, 11022 (2016).
990 23. Martin, M. Cutadapt removes adapter sequences from high-throughput sequencing reads.
991 *EMBnet.journal* **17**, 10–12 (2011).
992 24. Krueger, F. & Andrews, S. R. Bismark: a flexible aligner and methylation caller for
993 Bisulfite-Seq applications. *Bioinformatics* **27**, 1571–1572 (2011).
994 25. Schultz, M. D. *et al.* Human body epigenome maps reveal noncanonical DNA methylation
995 variation. *Nature* **523**, 212–216 (2015).
996 26. Frankish, A. *et al.* GENCODE reference annotation for the human and mouse genomes.

997 *Nucleic Acids Res.* **47**, D766–D773 (2019).
998 27. Wolf, F. A., Angerer, P. & Theis, F. J. SCANPY: large-scale single-cell gene expression
999 data analysis. *Genome Biol.* **19**, 15 (2018).
1000 28. Wolock, S. L., Lopez, R. & Klein, A. M. Scrublet: Computational Identification of Cell
1001 Doublets in Single-Cell Transcriptomic Data. *Cell Syst* **8**, 281–291.e9 (2019).
1002 29. Khan, A. *et al.* JASPAR 2018: update of the open-access database of transcription factor
1003 binding profiles and its web framework. *Nucleic Acids Res.* **46**, D260–D266 (2018).
1004 30. Bailey, T. L., Johnson, J., Grant, C. E. & Noble, W. S. The MEME Suite. *Nucleic Acids*
1005 *Res.* **43**, W39–49 (2015).
1006 31. McLean, C. Y. *et al.* GREAT improves functional interpretation of cis-regulatory regions.
1007 *Nat. Biotechnol.* **28**, 495–501 (2010).
1008 32. Hie, B., Bryson, B. & Berger, B. Efficient integration of heterogeneous single-cell
1009 transcriptomes using Scanorama. *Nat. Biotechnol.* **37**, 685–691 (2019).
1010

Extended data figure legends

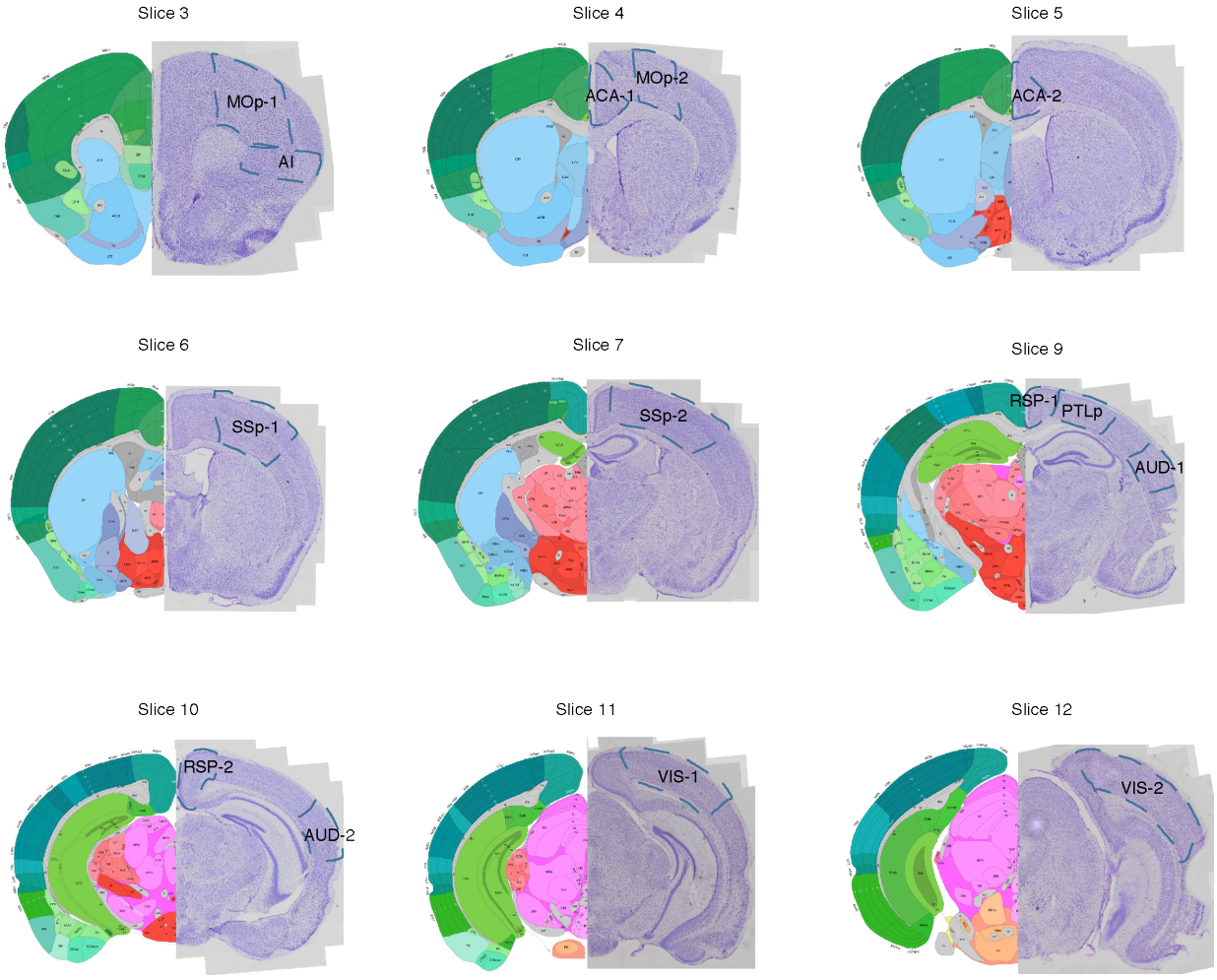

Extended Data Fig. 1 Source region dissection maps. The posterior views of dissected slices are shown. The slices correspond to Allen Reference Atlas level 33~39 (slice 3), 39~45 (slice 4), 45~51 (slice 5), 51~57 (slice 6), 57~63 (slice 7), 69~75 (slice 9), 75~81 (slice 10), 81~87 (slice 11), and 87~93 (slice 12), respectively.

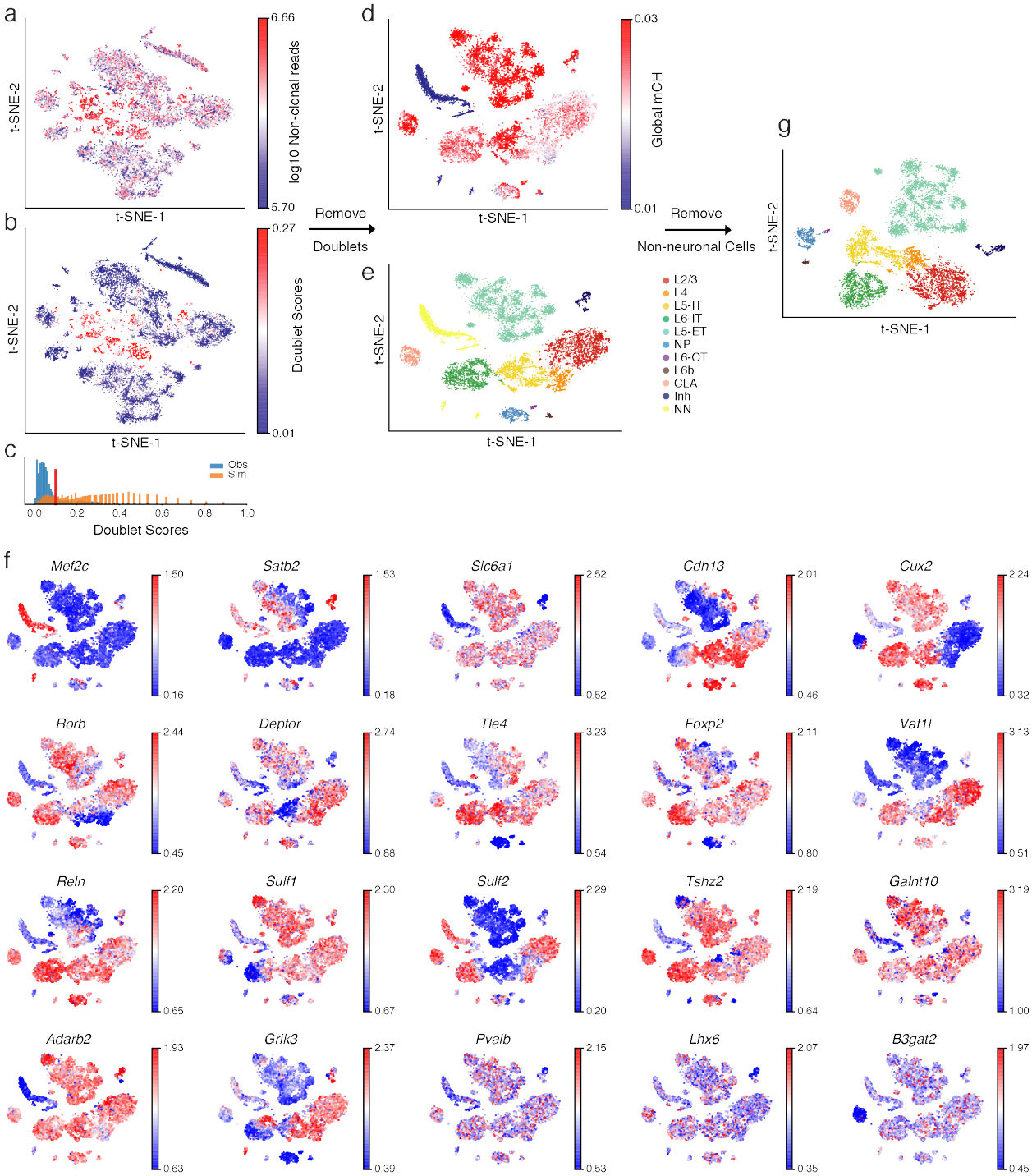

Extended Data Fig. 2 Removing potential doublets and non-neuronal cells. t-SNE of cells after quality control (n=16,971) colored by number of non-clonal reads (a) and predicted doublet scores (b). (c) Distribution of doublet scores for real cells (blue) and simulated doublets (orange). t-SNE of cells after removing doublets (n=13,414) colored by global mCH (d), cluster labels (e), and

1023 normalized gene-body mCH level of known cell type gene markers (f). Cells with low global mCH

1024 level are usually non-neuronal cells. t-SNE of single neurons (n=11,827) colored by the cluster

1025 labels (g). NN represents non-neuronal cells.

1026

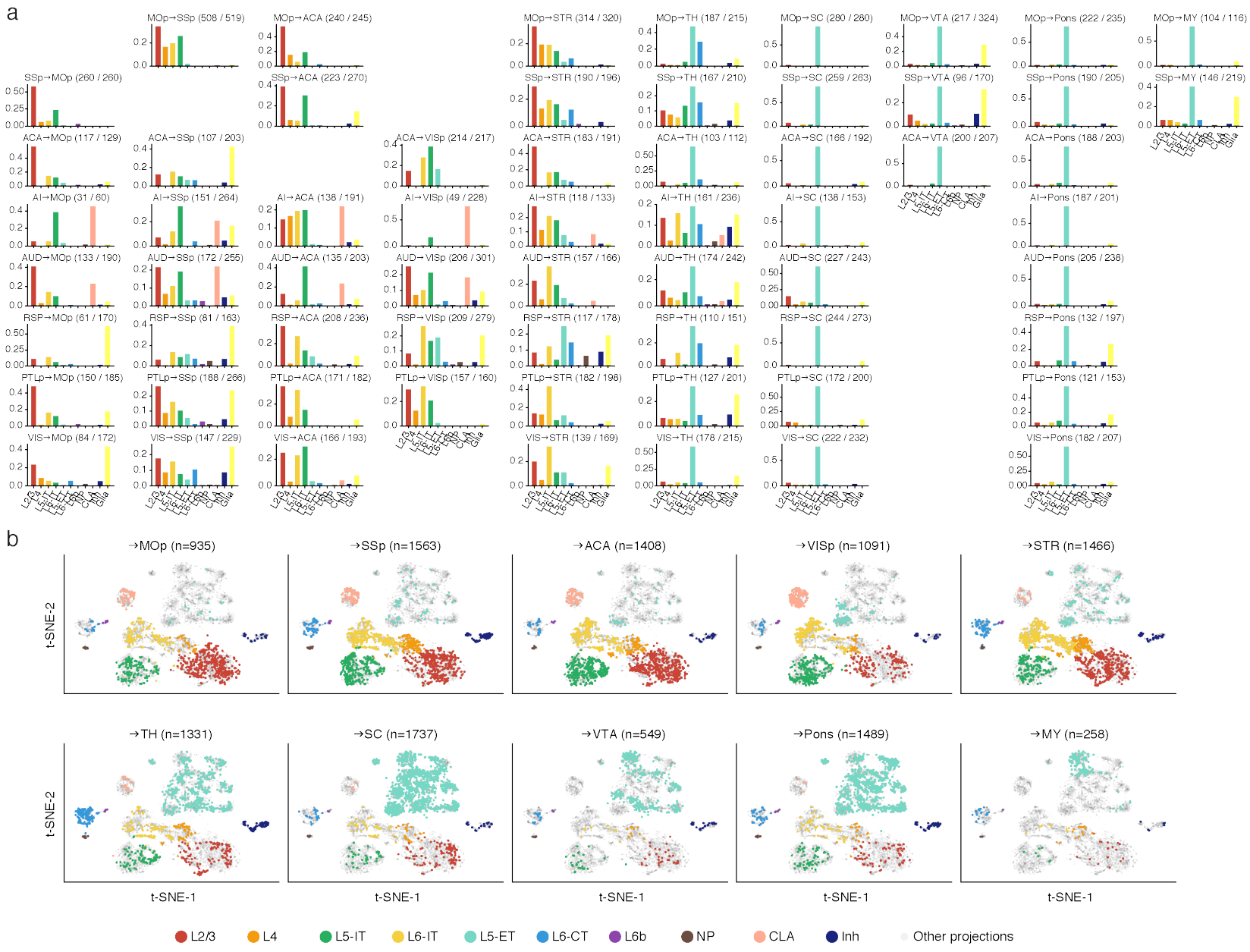
a
MOp→SSp (508 / 519)
MOp→ACA (240 / 245)
MOp→STR (314 / 320)
MOp→TH (187 / 215)
MOp→SC (280 / 280)
MOp→VTA (217 / 324)
MOp→Pons (222 / 235)
MOp→MY (104 / 116)
SSp→MOp (260 / 260)
SSp→ACA (223 / 270)
SSp→STR (190 / 196)
SSp→TH (167 / 210)
SSp→SC (259 / 263)
SSp→VTA (96 / 170)
SSp→Pons (190 / 205)
SSp→MY (146 / 219)
ACA→MOp (117 / 129)
ACA→SSp (107 / 203)
ACA→VISp (214 / 217)
ACA→STR (183 / 191)
ACA→TH (103 / 112)
ACA→SC (166 / 192)
ACA→VTA (200 / 207)
ACA→Pons (188 / 203)
AI→MOp (31 / 60)
AI→SSp (151 / 264)
AI→ACA (138 / 191)
AI→VISp (49 / 228)
AI→STR (118 / 133)
AI→TH (161 / 236)
AI→SC (138 / 153)
AI→Pons (187 / 201)
AUD→MOp (133 / 190)
AUD→SSp (172 / 255)
AUD→ACA (135 / 203)
AUD→VISp (206 / 301)
AUD→STR (157 / 166)
AUD→TH (174 / 242)
AUD→SC (227 / 243)
AUD→Pons (205 / 238)
RSP→MOp (61 / 170)
RSP→SSp (81 / 163)
RSP→ACA (208 / 236)
RSP→VISp (209 / 279)
RSP→STR (117 / 178)
RSP→TH (110 / 151)
RSP→SC (244 / 273)
RSP→Pons (132 / 197)
PTLp→MOp (150 / 185)
PTLp→SSp (188 / 266)
PTLp→ACA (171 / 182)
PTLp→VISp (157 / 160)
PTLp→STR (182 / 198)
PTLp→TH (127 / 201)
PTLp→SC (172 / 200)
PTLp→Pons (121 / 153)
VIS→MOp (84 / 172)
VIS→SSp (147 / 229)
VIS→ACA (166 / 193)
VIS→STR (139 / 169)
VIS→TH (178 / 215)
VIS→SC (222 / 232)
VIS→Pons (182 / 207)
L2/3 L4 L5-IT L6-IT L5-ET L6-CT L6b NP CLA Inh Glia
b
→MOp (n=935)
→SSp (n=1563)
→ACA (n=1408)
→VISp (n=1091)
→STR (n=1466)
→TH (n=1331)
→SC (n=1737)
→VTA (n=549)
→Pons (n=1489)
→MY (n=258)
t-SNE-2
t-SNE-1
L2/3
L4
L5-IT
L6-IT
L5-ET
L6-CT
L6b
NP
CLA
Inh
Other projections

1027

1028 **Extended Data Fig. 3 Cell type composition of all projections.** (a) The proportion of cells projecting from each source region (row)
1029 to each target region (column) in all clusters including non-neuronal cells. (b) t-SNE of neurons (n=11,827) projecting to each IT target
1030 (top) and ET target (bottom). The cells projecting to the target were colored by clusters and cells projecting to all other targets were
1031 greyed.
1032

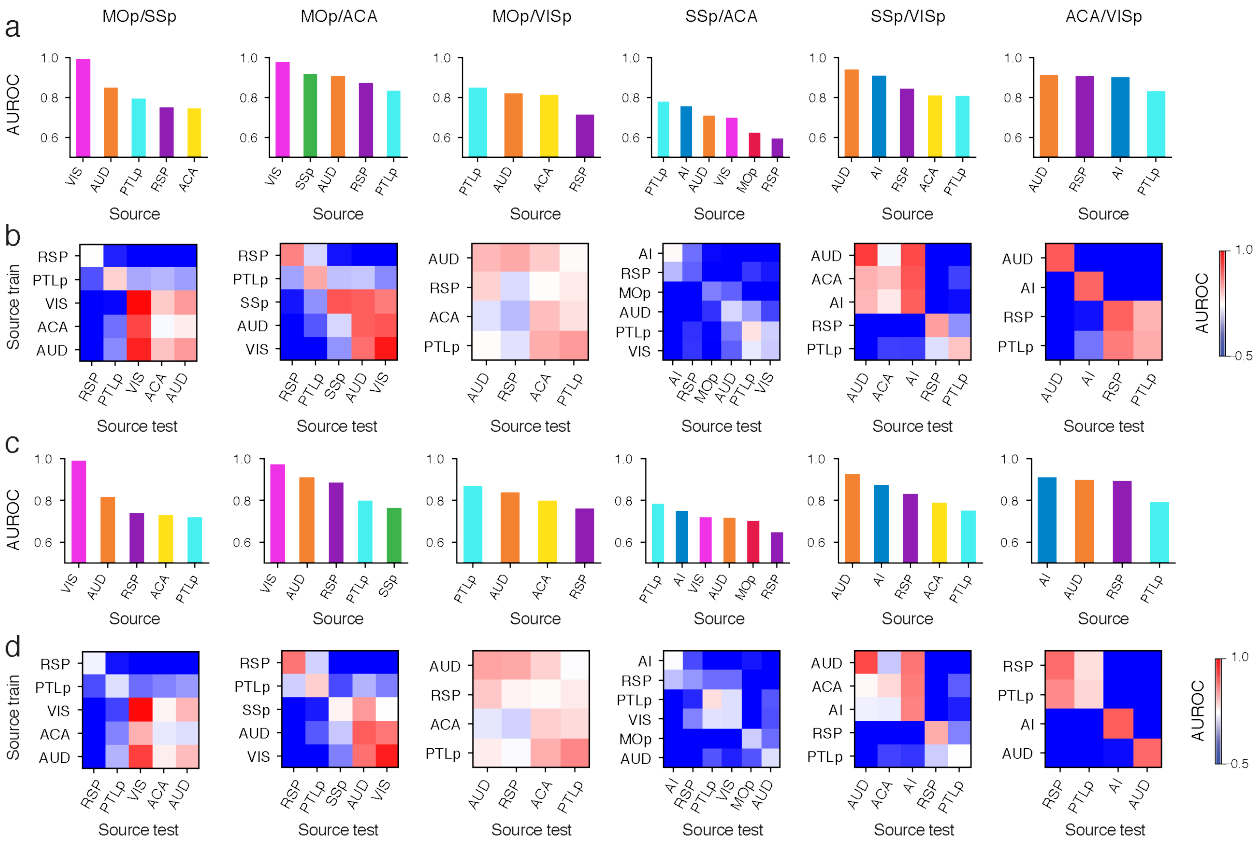

Extended Data Fig. 4 AUROC of cortical target pairs within and cross source regions. AUROC of models trained and tested in the same source region (a, c) or models tested in all source regions after trained in each one of them (b, d) using gene body (a, b) or 100 kb bin (c, d) mCH as features. The values in (a) and (c) correspond to the diagonals of (b) and (d) but ordered decreasingly.

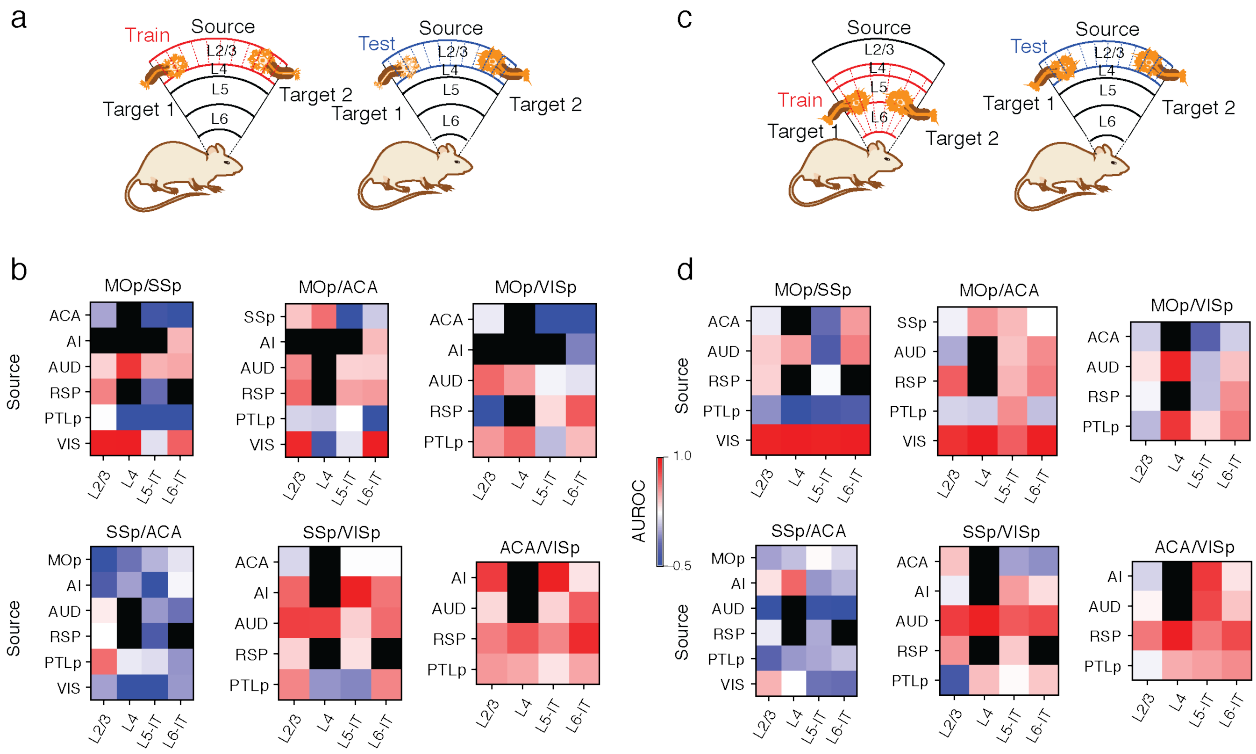

Extended Data Fig. 5 AUROC of cortical target pairs within and cross clusters. Demonstration of training and testing data for within layer prediction (a) and cross layer prediction (c). In (a), the models were trained and tested in the same layer with different replicates. In (c), the testing sets were the same as (a), but the models were trained in all other layers. AUROC of within layer prediction (b) or cross layer prediction (d). 100 kb-bin level mCH were used for all the predictions.

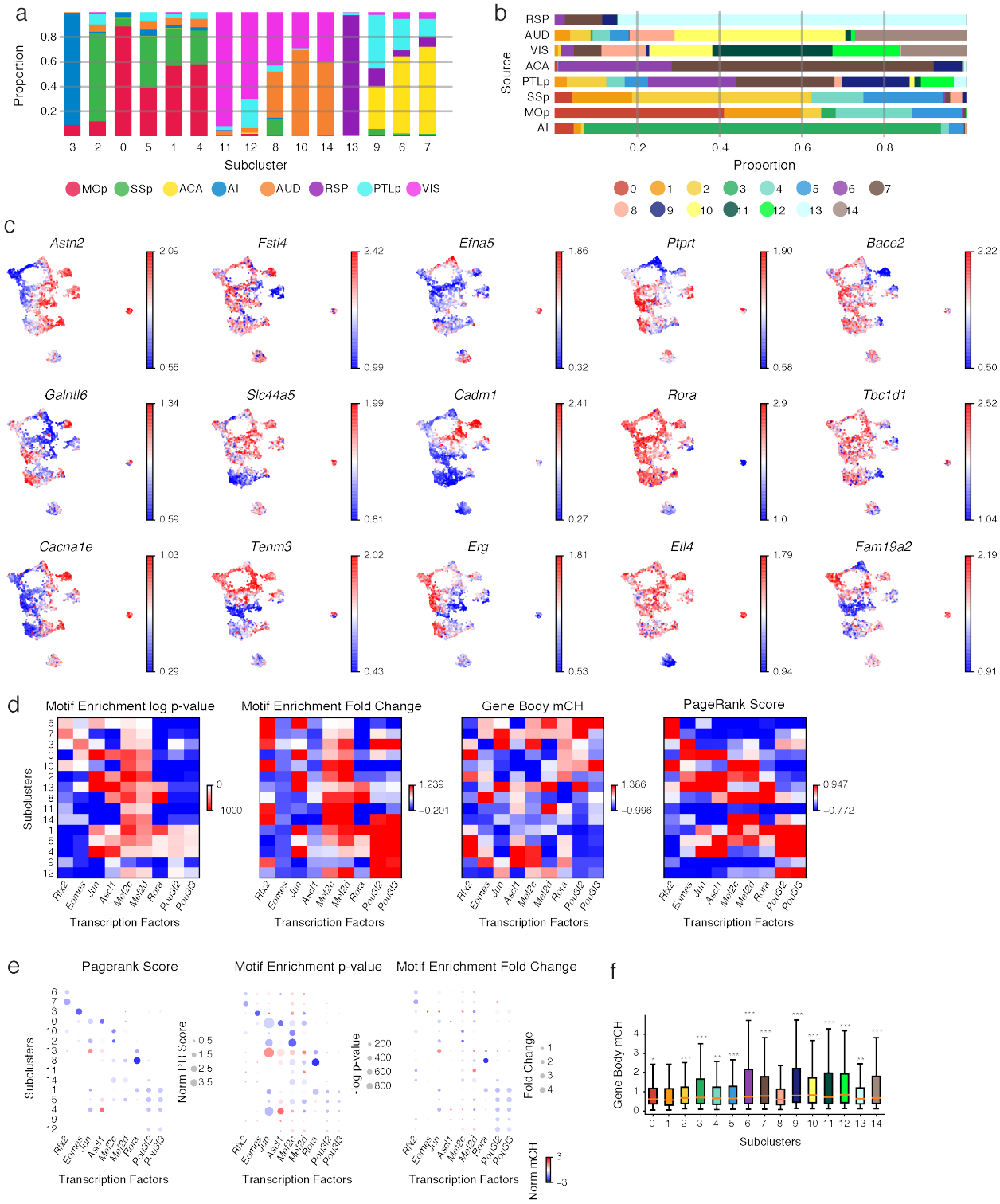

Extended Data Fig. 6 Signature genes and TFs of L5-ET subclusters. (a) Proportion of cells from all source regions in each subcluster. (b) Proportion of cells in all subclusters from each source region. (c) t-SNE of L5-ET cells (n=4,176) colored by the normalized gene-body mCH

level of subcluster gene markers. (d) Motif fold-change within DMRs, and motif enrichment *P* value within DMRs, gene-body mCH, and PageRank score of the example TFs in all L5-ET subclusters. (e) Gene body mCH (color) against PageRank score (size, left), motif enrichment *P* value (size, middle), and motif enrichment fold-change (size, right) for the example TFs in all L5-ET subclusters. (f) Gene body mCH in all clusters of *Rora* target genes identified in cluster 8. Significances were determined by comparing cluster 8 with each of the other clusters (two-sided Wilcoxon rank-sum test). * represents p<1e-2, ** represents p<1e-3, *** represent p<1e-4. The elements of all box-plots are defined as: center line, median; box limits, first and third quartiles; whiskers, 1.5× interquartile range.

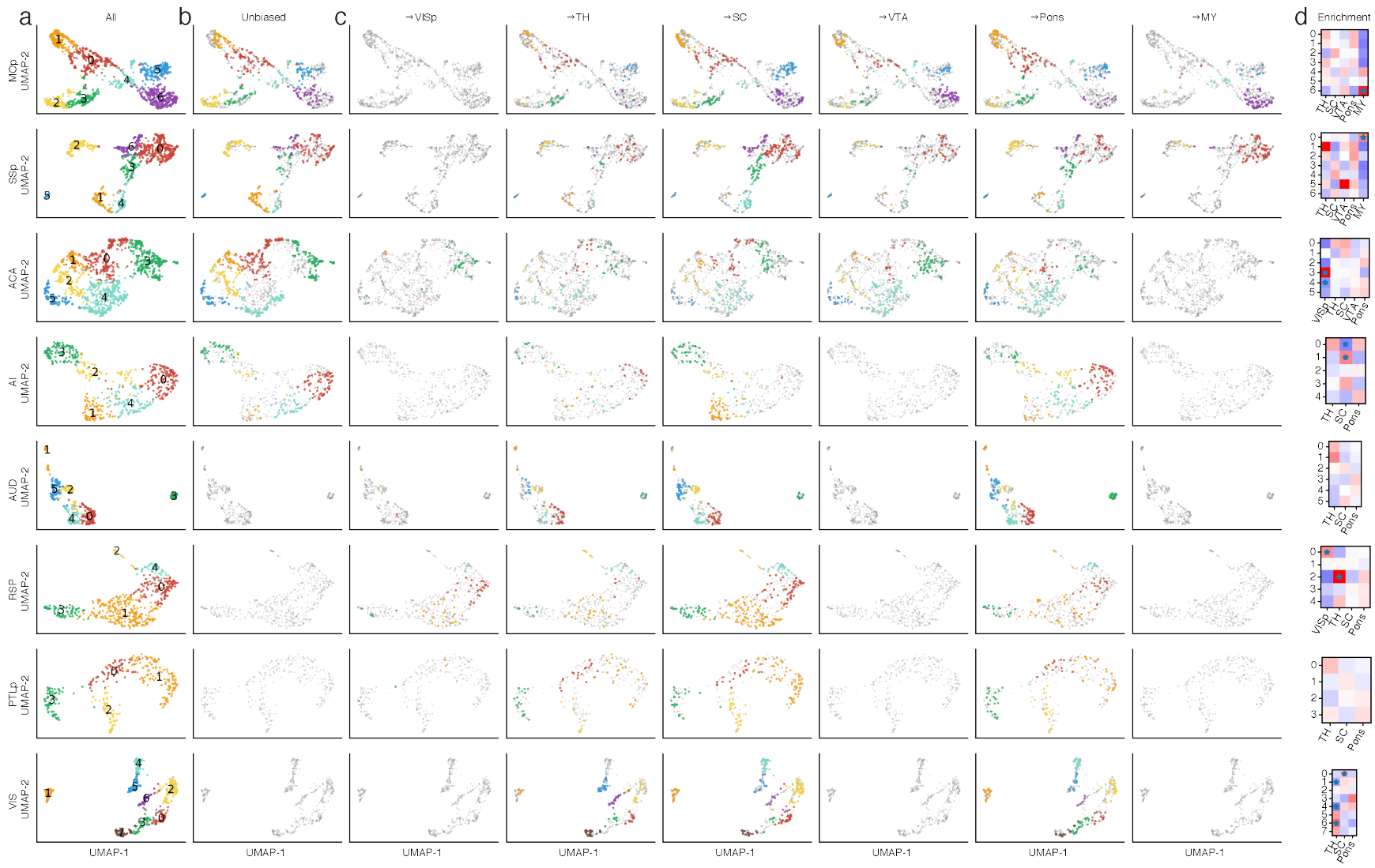

1062

1063 **Extended Data Fig. 7 Enrichment of different projections in L5-ET subclusters.** (a-c) t-SNE of L5-ET cells from each source region

1064 colored by subclusters. The colored cells are all cells (a), unbiased snmC-Seq cells (b), and cells projecting to each target (c). Other cells

1065 were greyed. (d) The enrichment of each projection in each L5-ET subcluster in each source. * represents FDR<0.05.

1066

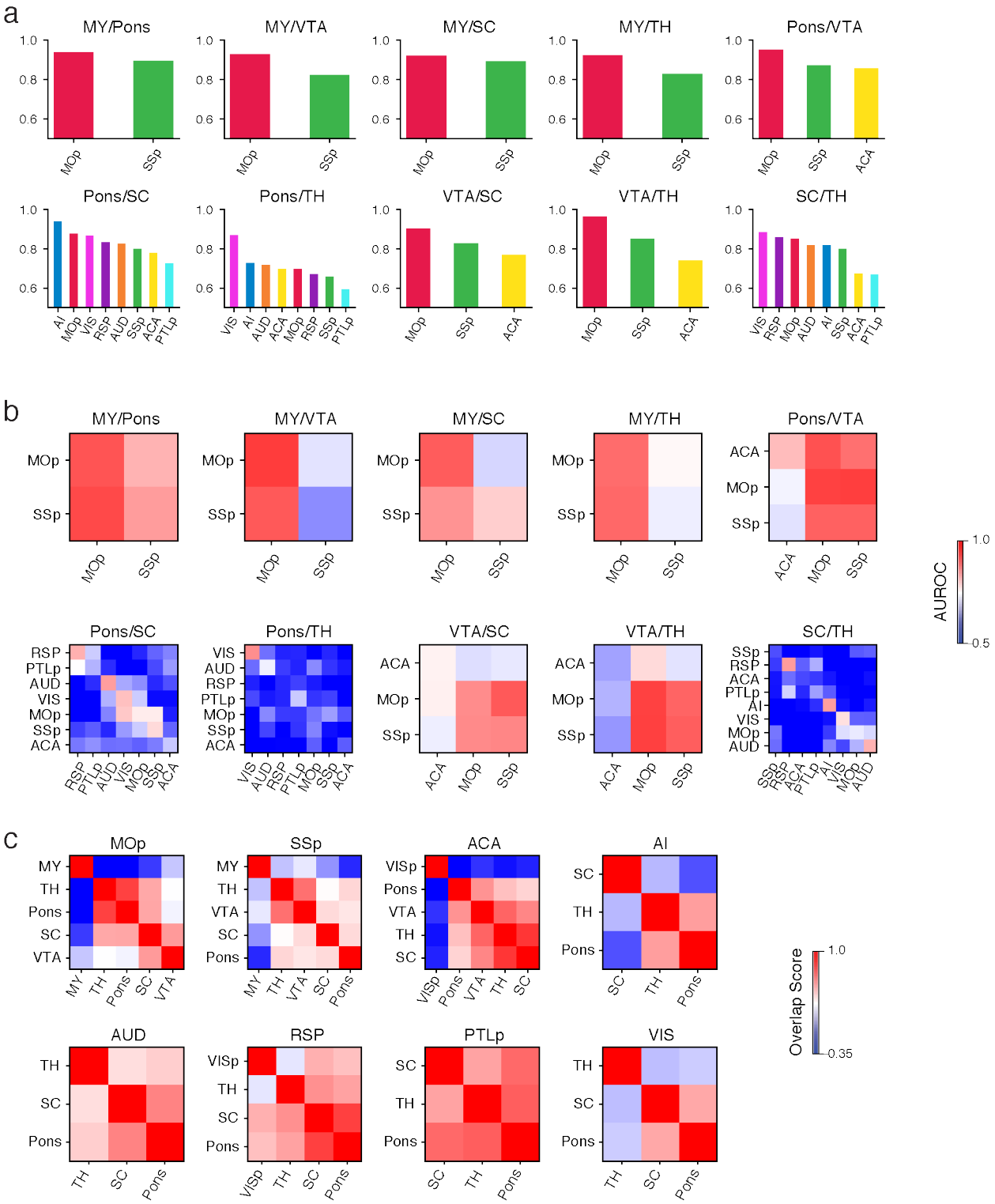

Extended Data Fig. 8 AUROC of ET target pairs within and cross source regions. AUROC of models trained and tested in the same source region (a) or models tested in all source regions

1070 after trained in each one of them (b) using 100 kb bin mCH as features. Training and testing sets
1071 were split by two-fold cross-validation in (a) to include AI, or split by replicates (b). (c) Overlap
1072 score between each pair of targets in each source region.
1073

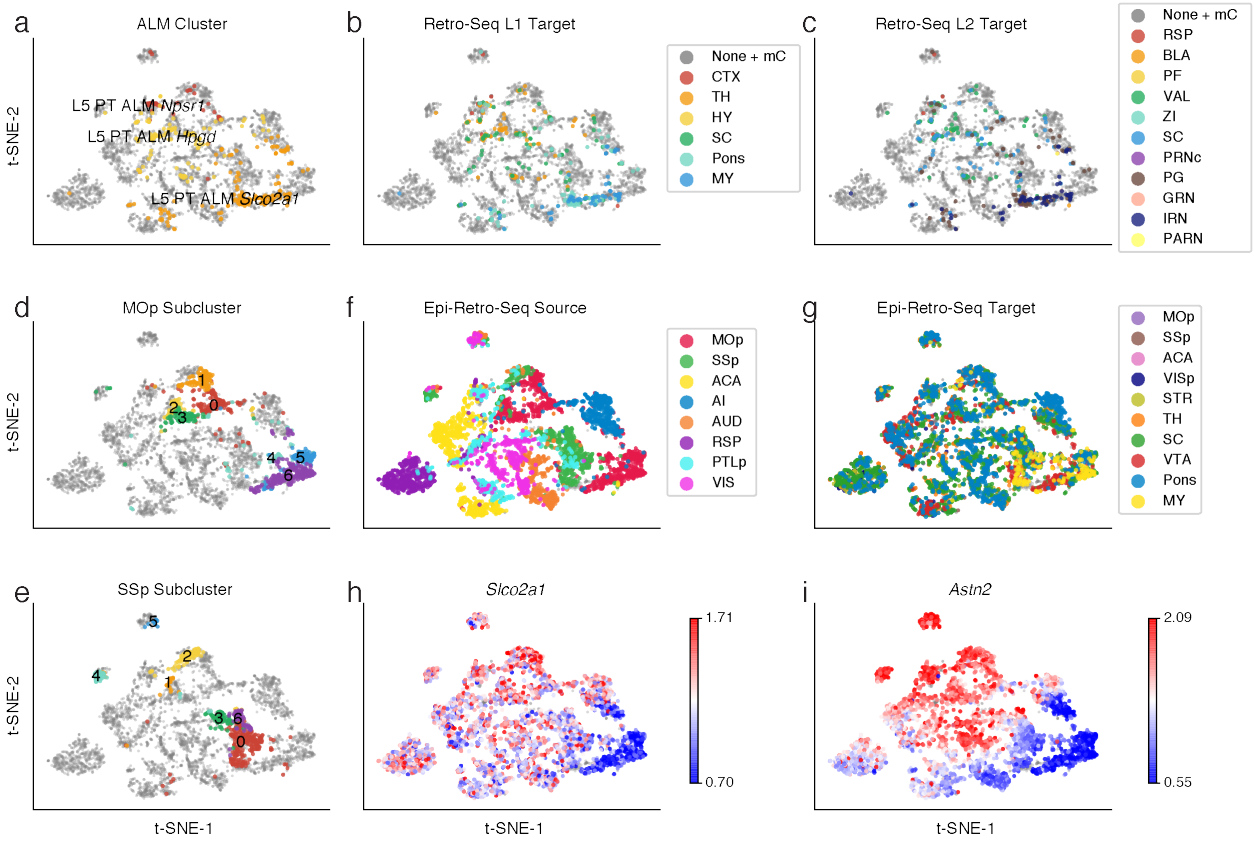

Extended Data Fig. 9 Integration of L5-ET cells from Epi-Retro-Seq and Epi-Seq. (a-c) L5-ET ALM cells in SMART-Seq (n=365) colored by clusters (a), major target regions (b), and detailed target regions (c). Epi-Retro-Seq cells were greyed. (d-i) L5-ET Epi-Retro-Seq cells from all source regions (n=4,176) colored by MOp subclusters (d), SSp subclusters (e), sources (f), targets (g), and gene body mCH of *Slco2a1* (h) and *Astn2* (i).

1081 **Supplementary Tables**

1082 **Supplementary Table 1. Epi-Retro-Seq injection information.**

1083 **Supplementary Table 2. Metadata and cluster assignment of 11,827 single neurons.**

1084 **Supplementary Table 3. CH-DMGs between IT neurons projecting to different target**

1085 **regions and GO enrichment.**

1086 **Supplementary Table 4. CH-DMGs between L5-ET subclusters and GO enrichment.**

1087 **Supplementary Table 5. CG-DMRs between L5-ET subclusters and target genes assigned by**

1088 **GREAT.**

1089 **Supplementary Table 6. CH-DMGs between L5-ET neurons projecting to different ET**

1090 **targets.**

1091 **Supplementary Table 7. Cell counting in double labeling experiments.**

1092